University of Twente
Enschede - The Netherlands

Spectral Shaping for Spectroscopy and Imaging

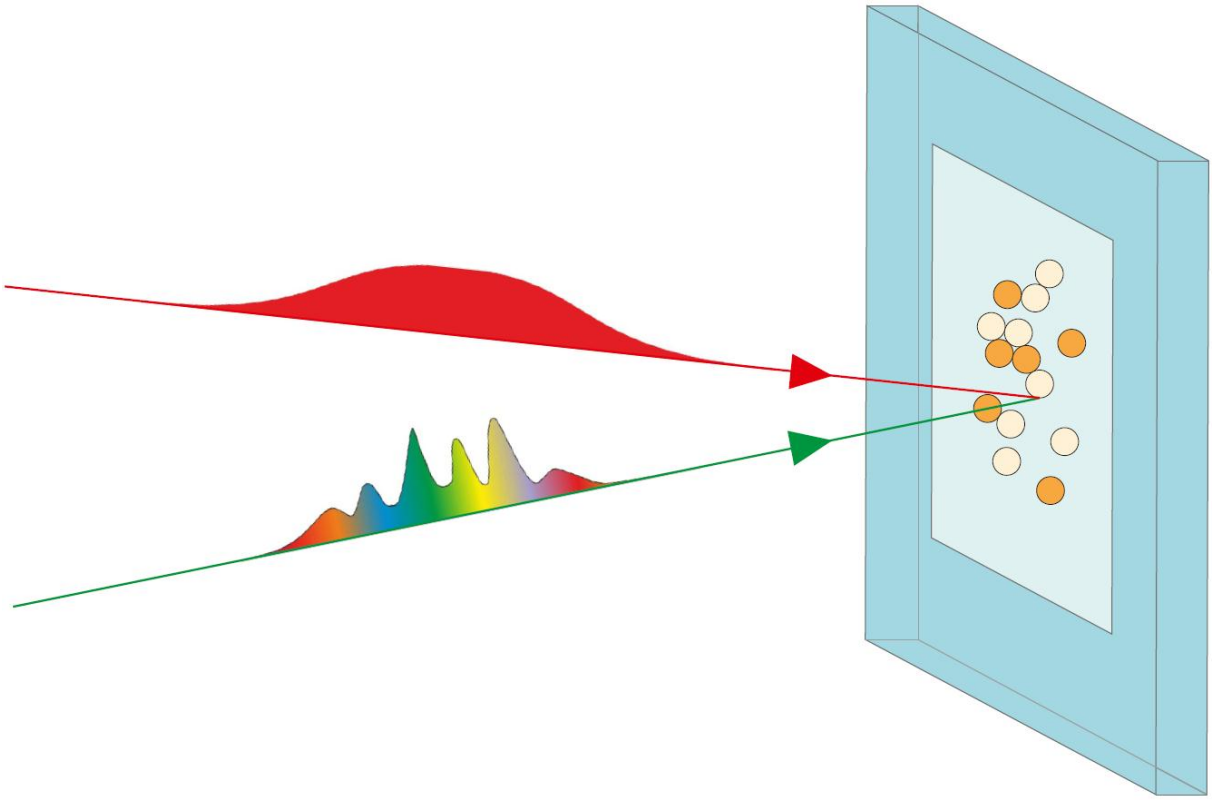

Frank Timmermans

Spectral Shaping for Spectroscopy and Imaging

For the title Master of Science
F.J. Timmermans
February 14, 2013

Optical Sciences
MESA+ Institute for Nanotechnology
Faculty of Science and Technology
University of Twente
Enschede
The Netherlands

Advisor

Dr. A.C.W. van Rhijn	Optical Sciences, University of Twente
Dr. ir. H.L. Offerhaus	Optical Sciences, University of Twente

Graduation committee

Prof. Dr. J.L. Herek	Optical Sciences, University of Twente
Dr. ir. H.L. Offerhaus	Optical Sciences, University of Twente
Dr. C. Blum	Nanobiophysics, University of Twente

Summary

This thesis describes developments that have been made on two applications of spectral shaping for imaging and spectroscopic analysis. The first application is based on coherent anti-Stokes Raman scattering (CARS). CARS provides label free chemical selectivity based on a compound's vibrational resonances, it is often used as a chemically selective imaging tool. The CARS signal is, through the anti-Stokes shift, free from one photon fluorescence background. In our system CARS is used for the detection of compounds with vibrational resonances in the fingerprint region 2800 cm^{-1} to 3200 cm^{-1}. By using spectral shaping we are able to remove non-resonant background from our signal and obtain an enhanced contrast for specific compounds.

Our images are obtained through detection of the integrated CARS signal on a silicon photodiode and scanning the sample through the lasers' focal volume with a XZ piezo driven scanning stage. By measuring the integrated intensity we have obtained efficient signal detection while chemical selectivity is obtained through selective excitation with the applied phase profiles. Imaging experiments have been performed on samples containing plastic beads such as polystyrene (PS) and Poly(methyl methacrylate) (PMMA) and on flow cells containing liquids such as ethanol, acetone and toluene. This work is a continuation of the project presented by Alexander C.W. van Rhijn[1].

In the second application, described in this thesis, spectral shaping is used in combination with a linear sample interaction and a nonlinear detector to obtain chemical specificity. It is commonly accepted that spectral shaping can only be used for spectroscopic analysis in combination with a nonlinear sample interaction. We however present proof of principle experiments in which dispersion in the sample is exploited so that in combination with a phase shape and detection of the two photon signal chemical information is obtained. These results could be extended to an imaging technique based on a linear sample interaction. With this method there is no need for focussing of light in the sample thus lowering the chance of damaging the sample. Detection is done on the integrated spectrum on a photodiode after excitation of second harmonic light in a nonlinear crystal. This work has been submitted to Optics Letters.

Contents

1. Introduction

The effect of spectral shaping and its effect on light matter interactions are a fundamental concept in this thesis. The aim of this work is to present new techniques and improvements on existing techniques for microspectroscopic imaging. There is a lot of interest in label free chemically selective imaging and in the last century a lot of research has been performed on microscopic and microspectroscopic imaging.

1.1 Microscopy

Lenses came into widespread use in the late 13th century, this was later used by Antonie van Leeuwenhoek in the 17th century to create optical microscopes. These microscopes were able to magnify images more than 200 times, and as such they were a huge improvement over the standards of that time. Van Leeuwenhoek's research was focused on imaging biological samples, such as bacteria and infusoria (small aquatic creatures). His results popularized the use of microscopes in biological applications.

In the last century fluorescence microscopy has been used to provide enhanced contrast for images in optical microscopy[2]. In these methods, fluorescent dyes are added to the sample. The fluorescence from these dyes is used instead of, or in addition to, absorbed and reflected light, in order to create an image of the sample. These dyes are excited by illuminating the sample with light so that fluorescence is emitted. The light is absorbed by the dye, bringing it in an electronic excited state. Subsequently the molecule will relax to a lower excited vibrational state, before returning to the ground state via the emission of a photon. The emitted light is of a longer wavelength and can be isolated from the excitation light through the use of a dichroic filter.

The Dutch physicist Frits Zernike was awarded the Nobel prize for the invention of phase contrast microscopy[3]. This method was developed in 1930 and in the 1940's the first few phase contrast microscopes were used in biomedical applications. Contrast is obtained through refractive index differences in the sample that give rise to phase differences on the transmitted light. This light is combined with a reference beam and interferes constructively or destructively.

In 1928 Raman scattering was discovered by the Indian physicist C.V. Raman[4]. In this process light scatters inelastically from a molecule resulting in an energy transfer between the light field and the molecules vibrational states. Chemical information of the sample is obtained by measuring the intensity and wavelength shift of the scattered light which gives a Raman spectrum. Since the Raman spectrum is specific for molecules this can be used for identification of sample compounds. A drawback of Raman spectroscopy is that the signal is very weak. Under average circumstances, a Raman scattering event occurs only once for every 10^7 Rayleigh scattering events. For this reason several nonlinear scattering processes have been investigated that enhance the Raman signal.

After the development of the laser and the accidental discovery of stimulated Raman scattering (SRS) much research has been done on this process[5]. In SRS microscopy a sample is illuminated with a pump laser, as is done for spontaneous Raman scattering microscopy, but in addition a second (Stokes) laser is used. The second laser is operating at the Stokes frequency, which is the frequency of the pump minus the frequency of the molecular vibration. When these beams interact with the sample they drive the molecules to oscillate at the difference frequency $\Omega = \omega_P - \omega_S$. In this process one pump photon is destroyed and one Stokes photon is generated leaving the molecule in a vibrational excited state. Under average conditions the SRS process gives a signal that is greatly enhanced compared to the signal obtained from spontaneous Raman spectroscopy.

In 1964 coherent anti-Stokes Raman scattering (CARS) was first reported[6] during a study on nonlinear third order optical phenomena. In the following decade not much research was done into CARS because of the need of high peak power tunable pulsed laser sources. Renewed interest in CARS came in 1974[7] when these laser sources became more widely available. The first CARS

microscope was created in 1982[8]. CARS is a nonlinear process that, like SRS, provides contrast based on vibrational resonances. CARS uses three excitation beams: a pump, Stokes and probe laser and creates its signal frequency at $\omega_{CARS} = \omega_{Pump} - \omega_{Stokes} + \omega_{Probe}$. In many situations the pump and probe fields are chosen to be degenerate so that only two lasers are necessary.

1.2 Phase and spectral shaping

Modifying (or shaping of) the phase of ultrashort light pulses is an important concept in this thesis. For a wave of light of a single frequency, the phase corresponds to the position of a full oscillation at a certain point in time. Ultrashort light pulses consist of many light waves of different frequencies. When at a certain point in time the phase of all these independent waves is equal the waves interfere constructively resulting in a very short and intense pulse of light. Figure 1.1 shows a simplified image of this process. This principle, called mode locking, is used in many lasers to create femtosecond pulses[9]. The constructive interference occurs with a regular time interval resulting in a train of pulses. In between consecutive pulses the intensity drops due to destructive interference. For shorter light pulses it is necessary to combine more frequencies, and therefore a broader spectrum. The larger range of frequency components results in a smaller time interval where these waves are in phase and the combination of more waves gives higher pulse intensity, assuming equal mode intensity.

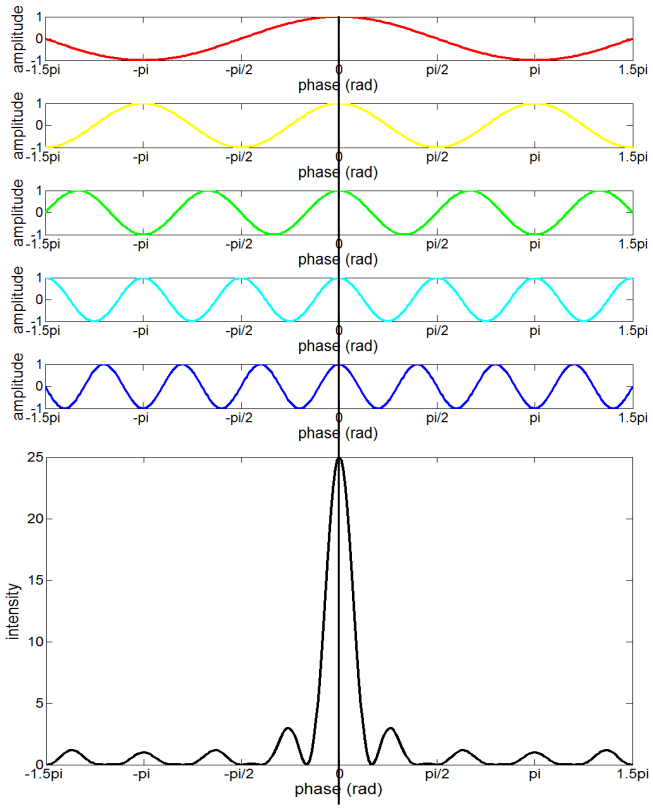

Figure 1.1: *Wave interference for an ultrashort pulse. The top picture shows five individual waves with different frequencies these represent the light fields. The bottom picture shows the modulus squared of the sum of these waves. When all waves are in phase the result is a short intense pulse.*

It is possible to control the spectral phase of the light pulses with a spatial light modulator (SLM). By controlling the spectral phase, one has a large influence on the temporal character of light as the waves are generally not all in phase with different phase profiles. The spectral shaping of light pulses thus results in a complex and temporally broader pulse, which is more intuitively shown in Figure 1.2, where an analogy with a musical scale is made. Hitting several notes at the same time results in the shortest possible pulse containing all frequency components, when the notes are played in a sweep the result is comparable to a chirped pulse. When a melody is played the notes are arranged in a complex order and in the time domain the result is also a complex melody. Changing the temporal character of

light is used in the field of coherent control to influence and measure nonlinear optical processes[10]. In this work the shaping is used to match the phase of the light with the phase of molecular vibrations. This can provide an enhanced or more specific signal from a certain compound. Of course for these processes we need precise control over the applied phase profiles.

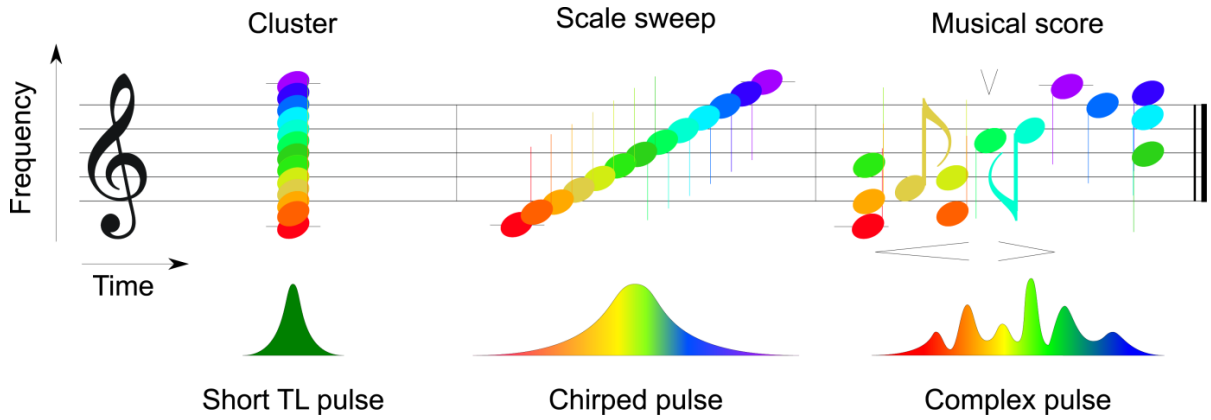

Figure 1.2: *Analogy with a musical scale to represent the effect of spectral shaping on the temporal behavior of the light pulse*[11].

1.3 Thesis overview

In this thesis I describe work and improvements that have been made on our shaped broadband CARS setup. First the theoretical description of the CARS process and the shaping of ultrashort light pulses is given. Then the working principle of the setup will be discussed. I will describe how the system works and which developments have been made. Finally we discuss the possibility to obtain a selective excitation of different compounds and mixtures.

We have also investigated a new spectroscopic method, where we combine the effect of spectral phase shaping and a purely linear interaction with a sample to obtain chemically specific information about the sample. I will discuss the working principle of the method, how the setup works and the theoretical background. Furthermore numerical and experimental results will be presented and the possibilities and challenges of the method are discussed. An overview of the different chapters in this thesis is given below.

Chapter 2 covers the theoretical background necessary to understand CARS spectroscopy. The fundamentals of narrowband and broadband CARS are covered, as well as the use of spectral shaping to influence the CARS signal of individual compounds. The origin of the non-resonant background will be discussed and I will describe how this background can be removed from our signal by using spectral shaping.

Chapter 3 contains a description of the setup used for the CARS experiments. It covers the lasers that are used and how the pulse trains from these lasers are synchronized, details about the spectral shaping that is performed on one of the pulse trains are discussed. The resulting signal is detected with lock-in detection where we use an acousto-optic modulator (AOM) for amplitude modulation. A new sample scanning stage that was added to the system is described. This stage provides a larger sample scanning area and can carry a larger weight, which is necessary for the measurements on liquids in a flow cell.

Chapter 4 covers the numerical optimization for phase shaped CARS experiments, and how we recover the complex molecular response of different compounds from a Raman Spectrum. An optimized phase profile can be numerically obtained to remove non-resonant background and gain an enhanced contrast for a compound of interest. This chapter also covers how we perform optimization for multi-compound mixtures and how we are able to optimize for resonant mixing terms between the compounds.

Chapter 5 contains results that are obtained for CARS imaging. We present selective imaging with non-resonant background removal of different compounds. The used phase shapes are obtained in either an experimental or numerical optimization process. CARS imaging has been performed on samples containing plastic beads or on flow cells containing different liquids.

Chapter 6 covers a new spectral phase shaping technique that can be used to obtain chemical information based on a linear sample interaction. A theoretical background, in which we cover how the phase delay in the compound can be obtained from an absorption spectrum and Sellmeier equations is provided, as well as an explanation of how the chemically specific information is obtained. A description and overview of the setup is also provided.

Chapter 7 contains numerical and experimental results of the technique covered in chapter 5. The use of phase 'landscapes', that contain signal dependence on the applied phase profiles along different projections, are highlighted. The simulated and experimental landscapes are compared and discussed. Furthermore remaining challenges and future possibilities are discussed.

2. Coherent anti-Stokes Raman scattering

2.1 Molecular vibrations

Molecules can move in many ways, such as rotations and vibrations. More complex molecules have a larger number of different potential motions. This total number of motions is called the degrees of freedom and is equal to 3 times the total number of atoms in the molecule. Of these 3N degrees of freedom, 3 originate from a translation in the x, y and z direction of the full molecule. Another 3 degrees generally originate from rotations of the full molecule around the x, y and z axes[10]. The remaining degrees of freedom correspond to vibrational movements in the molecule where different parts move with respect to each other. To visualize these vibrational modes one can imagine the molecule as a system of masses connected by springs. The vibrational modes of water are shown in Figure 2.1[12].

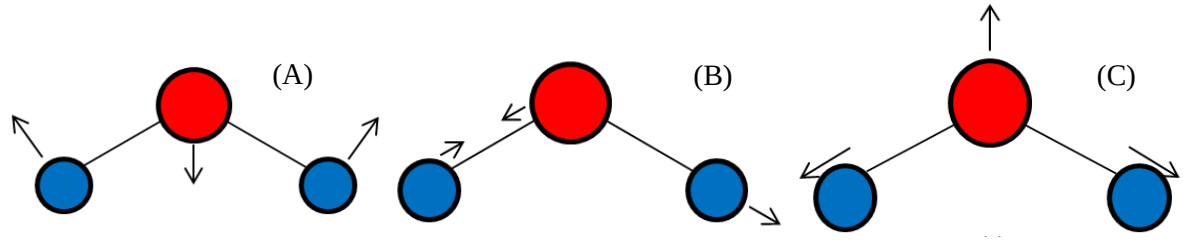

Figure 2.1: *Three Vibrational modes of water. (A) H_2O Bending mode, (B) H_2O Anti symmetric stretch mode, (C) H_2O Symmetric stretch mode*

For a molecule symmetric around a rotational direction like CO_2 there are only 2 rotational modes. This is because a rotation around the axis in line with the atoms does not change the molecule. Since there are still 3N degrees of freedom there are now 3N-5 vibrational modes. For CO_2 these modes are presented in Figure 2.2[12].

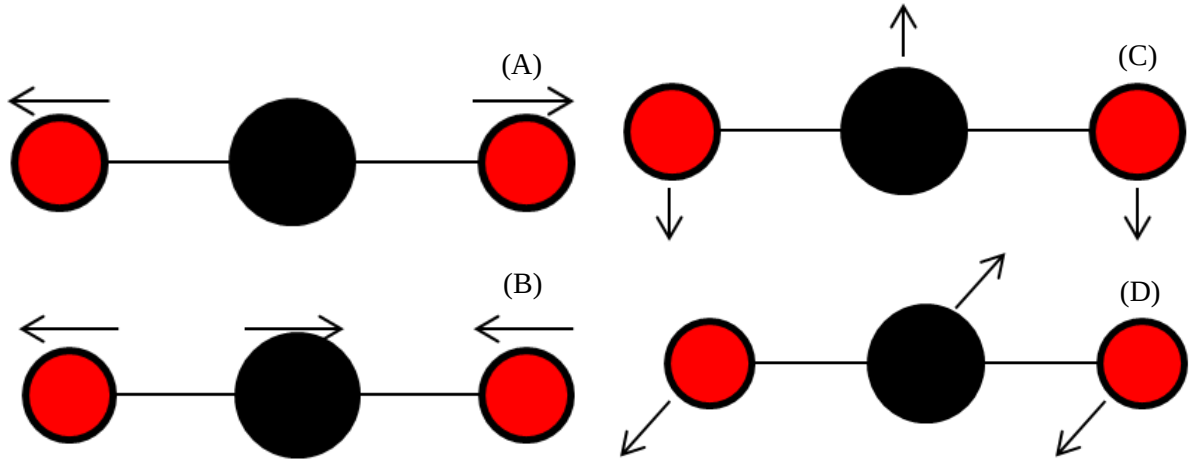

Figure 2.2: *Vibrational modes for CO_2. (A) Symmetric stretch mode, (B) Anti symmetric stretch mode, (C and D) are degenerate bending modes one is in plane and the other is out of plane with the paper.*

The vibrational resonance frequencies can be calculated for these molecules. The resonance frequency depends on the mass of the atoms involved and the bonding strength between these atoms. Using Hooke's law the resonance frequencies and the corresponding energies can be calculated[13].

2.2 Vibrational spectroscopy

2.2.1 Spontaneous Raman scattering

Raman scattering is a form of scattering in which energy is transferred between the molecules vibrational states and the light field. In the case of Stokes scattering, shown in Figure 2.3 (B), the molecule is left in an excited state and the scattered photon is of a lower frequency. A different process that can occur is anti-Stokes scattering, shown in Figure 2.3 (C). In this case the energy is transferred from a vibrational state to the light field, this process occurs less often as the molecule needs to be in a vibrational state before the scattering event occurs. Raman scattering can be used for spectroscopy, because the frequency of energy of the vibrational states depends on the weight of the atoms and bonding strength in a molecule. Hence the distribution of vibrational states is unique for every compound. By measuring the frequency shift of the excitation light it is possible to detect the strength and resonance frequency of the vibrations. As a result Raman scattering has been used in spectroscopy experiments[14][15]. However, only a very small fraction of the light undergoes inelastic scattering. In the vast majority of scattering events the light undergoes only Rayleigh scattering, as is shown in Figure 2.3 (A), in which the emitted light is of the same wavelength as the incoming light and no vibrational information can be obtained.

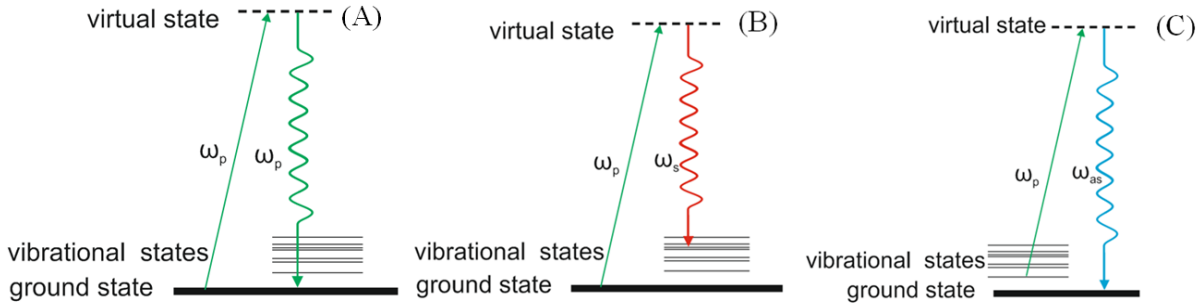

Figure 2.3: *(A) Rayleigh scattering. (B) Stokes Raman scattering. (C) Anti-Stokes Raman scattering*

Raman scattering differs from fluorescence since in the latter case absorption of light in an excited state is needed. In fluorescence, the molecule relaxes from its excited state to a lower state before reemitting a photon, this photon is emitted from a lower state and thus of a lower frequency compared to the incoming light. Fluorescence therefore can result in a background signal that can obscure the signals from Raman spectroscopy.

2.2.2 Stimulated Raman scattering

To enhance the signal that is obtained in Raman scattering at one particular frequency shift a second laser at that shift frequency can be used. This laser is used to stimulate the Raman scattering process and therefore this process is called stimulated Raman scattering (SRS), and has been successfully used for imaging[16]. The enhanced signal provided by SRS allows for much shorter imaging times. The energy diagram for SRS is shown in Figure 2.4. Generally two picosecond lasers are used, where the frequency of one of the lasers is scanned during the experiment. By scanning the laser frequency it is possible to scan the difference frequency between the two lasers over several vibrational resonances. When the difference frequency coincides with a vibrational resonance the SRS process occurs. As can be seen from Figure 2.4, in the SRS process the pump field loses one photon and the Stokes field gains one photon. The chemical information is thus obtained by looking at the intensity change in the two light fields and its dependence on the difference frequency between the two lasers.

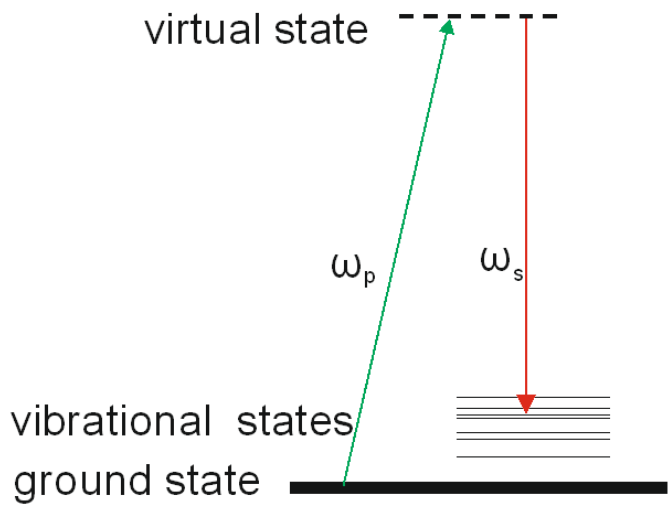

Figure 2.4: *Energy diagram stimulated Raman scattering*

Using SRS rather than spontaneous Raman scattering enhances the signal, but there can still be a fluorescent background signal from other molecules. Also for signals of weak resonances it is necessary to detect a small change in intensity in two intense laser fields. This is difficult compared to detecting a small signal on a zero intensity background as the laser field induces more noise. To circumvent this problem one can use the coherent anti-Stokes Raman scattering process.

2.3 Coherent anti-Stokes Raman scattering

Coherent anti-Stokes Raman scattering (CARS) is a nonlinear optical process that is primarily used for spectroscopy and imaging. The process is used to find the same vibrational resonances of a molecule as is done in Raman spectroscopy. CARS is a nonlinear process involving four light fields. In the CARS process a pump, stokes and probe field interact with a sample and generate an anti-Stokes shifted CARS field with frequency $\omega_{as} = \omega_p - \omega_s + \omega_{pr}$. In many systems the pump and probe fields are taken from the same laser source thus having an equal frequency. The energy diagram for the CARS process can be seen in Figure 2.5. The CARS signal is resonantly enhanced when the difference frequency of the pump and Stokes field ($\omega_p - \omega_s$) coincides with a vibrational resonance of the molecule. This allows us to find several vibrational resonances of the molecule by tuning the difference frequency between the pump and Stokes field. This process gives the vibrational spectrum of the molecule, which allows us to identify the molecule.

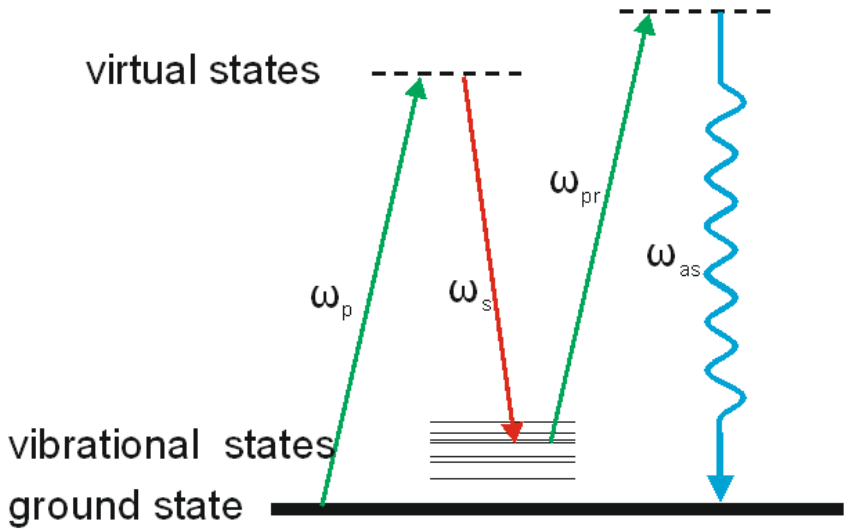

Figure 2.5: *CARS energy level diagram*

The main advantage of this process is that imaging can be performed orders of magnitude faster compared to Raman spectroscopy. Another advantage is that the detected light is blue shifted compared to the excitation laser fields, so there is no one photon fluorescence background. CARS microscopy was first used in1982[8] and is since then successfully used as a microspectroscopic imaging technique[17].

2.3.1 Broadband CARS

Another approach to CARS is to use a broadband pump or Stokes pulse instead of narrowband pulses. With the broadband excitation, multiple vibrational resonances can be excited simultaneously, so there is no need to tune the pump or Stokes field frequency. In multiplex[18] CARS a broadband Stokes laser is used. Other methods have been reported where the pump, Stokes and probe fields are taken from a single broadband laser[19], also known as single pulse CARS.

In our approach, a broadband pump and probe field is used (see Figure 2.6). The main advantage of this is that it provides mixing of resonances which is necessary for our spectral shaping technique, this is explained in more depth in chapter 2.5.1. The intensity relation for the CARS signal is described in formula (2.1)[20].

$$I_{CARS} \propto \left| \left(\left(E_P(\omega_P) \otimes E_S(\omega_S) \right) \cdot \chi^{(3)}(\omega) \right) \otimes E_{Pr}(\omega_{Pr}) \right|^2 \qquad (2.1)$$

The formula for the CARS intensity can be simplified for our implementation. Since the Stokes beam is narrowband, it can be approximated by a Dirac pulse in the frequency domain. As a result the convolution of the pump and Stokes fields gives a frequency shifted pump field. Furthermore the pump and probe fields in our setup are degenerate so that we get formula (2.2):

$$I_{CARS} \propto \left| \left(|E_P(\omega + \omega_S)| e^{i\varphi_p(\omega+\omega_s)} \cdot \chi^{(3)}(\omega) \right) \otimes |E_P(\omega)| e^{i\varphi_p(\omega)} \right|^2 \qquad (2.2)$$

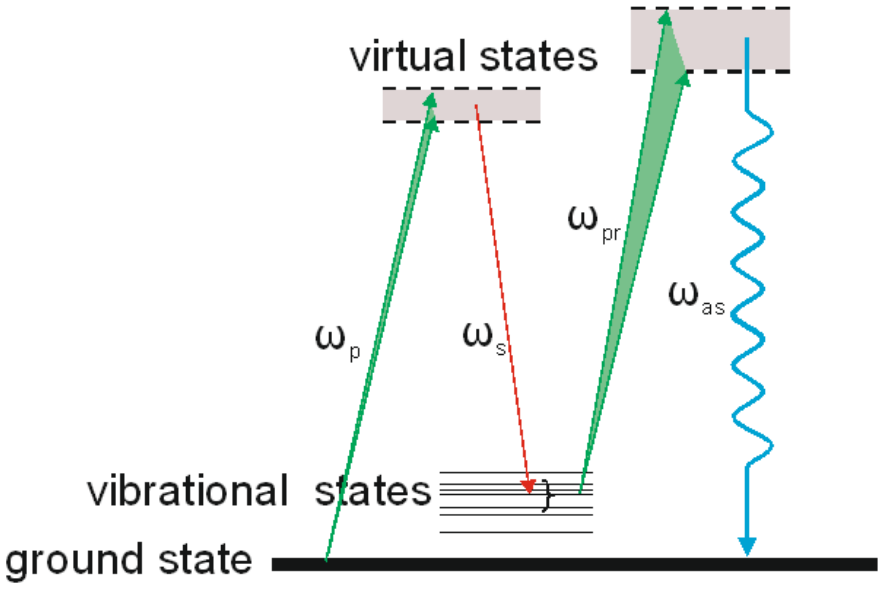

Figure 2.6: *Energy level diagram for broadband CARS*

A disadvantage of using a broadband probe laser is that the measured CARS spectrum is smeared out, this is as a result of the convolution presented in formula (2.2). However we obtain chemical selectivity through our spectral shaping technique as is explained in chapter 2.5.

2.3.2 Non-resonant background

Besides the resonant signal that is generated from the vibrational resonances, there is a non-resonant contribution to the CARS signal. This contribution comes from four wave mixing in a molecule without an interaction with a vibrational resonance as is shown in Figure 2.7. The result is a background signal at the anti-Stokes frequency that gives no chemical information about the molecule. Weak resonances can easily become indistinguishable when there are many surrounding molecules without vibrational resonances in the excited spectral region. The sensitivity in many CARS measurements is therefore limited by the ability to distinguish between the resonant and non-resonant signals. There are several methods that can be used to remove or suppress the non-resonant signal.

In time resolved CARS[21] a time delay is applied between the pump / Stokes pulse(s) and the probe pulse. The molecule will immediately relax from a virtual, while this takes longer for a vibrational state, so that a suitable time delay will remove the non-resonant background while preserving a part of the vibrational resonant signal. Polarization-sensitive detection is based on the different polarization properties of the resonant and non-resonant portions of the third order nonlinear susceptibility[22][23]. When using a linearly polarized pump and Stokes beam, the non-resonant signal can be greatly suppressed by varying the difference in polarization angle. Another method is vibrational phase contrast CARS[24] (VPC-CARS). The phase of the CARS field is measured with respect to the excitation fields. With this method the phase of the oscillators in the focal volume can be recovered. This allows for rejection of the non-resonant background as this has a zero difference in phase with respect to the input fields. In our system we use two measurements with different phase shaped pump and probe light. The two phase shapes are chosen such that they both influence the non-resonant contribution in the same way while they influence the resonant contributions differently. What follows is that the difference intensity contains only contributions of vibrational resonant molecules. This process is described in more detail in chapter 2.5.

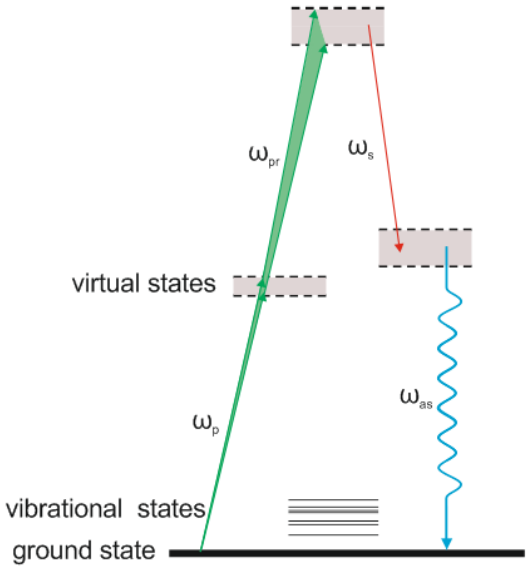

Figure 2.7: *Four wave mixing non-resonant background*

2.4 Third-order nonlinear susceptibility

We can describe the interaction between light and matter by the polarizability of the matter. The relation between the polarizability **P** and the electric field **E** can be described by a sum of the linear and higher order contributions. The higher order contributions describe processes involving multiple excitation photons. The polarizability is described with formula (2.3)[25]:

$$\bar{P} = \varepsilon_0 \bar{\bar{\chi}}^{(1)} \cdot \bar{E} + \bar{\bar{\chi}}^{(2)} \cdot \bar{E} \cdot \bar{E} + \bar{\bar{\chi}}^{(3)} \cdot \bar{E} \cdot \bar{E} \cdot \bar{E} + \cdots \quad (2.3)$$

The CARS process is driven by the pump, Stokes and probe fields, as this is a combination of three electric fields the CARS process depends on the third-order nonlinear susceptibility $\chi^{(3)}$. As was stated before the signal increases significantly when the probe and Stokes difference frequency coincides with a vibrational resonance, this is a result of the CARS intensity being proportional to the modulus squared of $\chi^{(3)}$, and $|\chi^{(3)}|$ increases strongly on resonance. The third-order nonlinear susceptibility of a single resonance can be approximated with a damped harmonic oscillator[20] as follows.

$$\chi_R^{(3)} = \frac{A_R}{\omega_R^2 - \omega^2 + 2i\gamma_R\omega} \quad (2.4)$$

Where ω is the driving frequency ($\omega_{pump} = \omega_{Stokes}$), ω_R is the resonance frequency and γ_R indicates the damping of the oscillator. The value of modulus $\chi_R^{(3)}$ increases significantly on resonance, when $\omega = \omega_R$, resulting in an enhanced CARS signal. There is also a non-resonant contribution through the interaction of the light fields with only virtual states, this is shown in Figure 2.7. This contribution is an addition to the resonant contributions. The total third-order nonlinear susceptibility can therefore be described as $\chi^{(3)} = \chi_R^{(3)} + \chi_{NR}^{(3)}$. The non-resonant background $\chi_{NR}^{(3)}$ is assumed to be constant in amplitude in the spectral region of interest so that it has a zero phase. Since a molecule typically contains multiple vibrational resonances the total function for $\chi^{(3)}$ becomes:

$$\chi^{(3)} = \chi_R^{(3)} + \chi_{NR}^{(3)} = \sum_R \frac{A_R}{\omega_R^2 - \omega^2 + 2i\gamma_R\omega} + \chi_{NR}^{(3)} \quad (2.5)$$

CARS is a coherent process in which the vibrational resonances oscillate in phase and interfere constructively[17]. As a result the CARS signal is proportional to the modulus squared of $\chi^{(3)}$. Because of this modulus squared dependence the signal is also affected by mixing between the resonant and non-resonant contributions of $\chi^{(3)}$.

$$\left|\chi^{(3)}\right|^2 = \left|\chi_R^{(3)} + \chi_{NR}^{(3)}\right|^2 = \left|\chi_R^{(3)}\right|^2 + \left|\chi_{NR}^{(3)}\right|^2 + 2\chi_{NR}^{(3)} Re\left(\chi_R^{(3)}\right) \quad (2.6)$$

Figure 2.8 A to H show some characteristics of a damped harmonic oscillator and the effect of a real valued offset (from the non-resonant background). We consider a damped harmonic oscillator with a resonance frequency of 3000 cm^{-1}, where the amplitude of the real part of the resonant contribution is normalized to 1 and the non-resonant amplitude is set at 0.6. Figure A, C, E and G show characteristics without non-resonant background. Figure B, D, F and H show characteristics with non-resonant background. Figure 2.8 (A and B) show the amplitude of the real and imaginary part of the resonance. Figure 2.8 (C and D) show the modulus squared of $\chi^{(3)}$. It can be seen that, in the presence of non-resonant background, the intensity is asymmetrically distributed in frequency and there is a dip in the intensity to the right side of the peak. This is an effect of the mixing between the resonant and non-resonant components. The intensity of a single resonance without background follows a damped harmonic oscillator function which is approximately symmetrical when $\omega_R \gg \gamma_R$. The phase of the oscillator is shown in Figure 2.8 (E and F). For a single resonance the phase follows the function of a negative π step centered at ω_R. With the presence of the background the mixing with the background the phase returns zero and does not reach the –π value. Figure 2.8 (G and H) show the relation between the real and imaginary amplitude of the susceptibility. Due to the four wave mixing background the figure is shifted along the real axis.

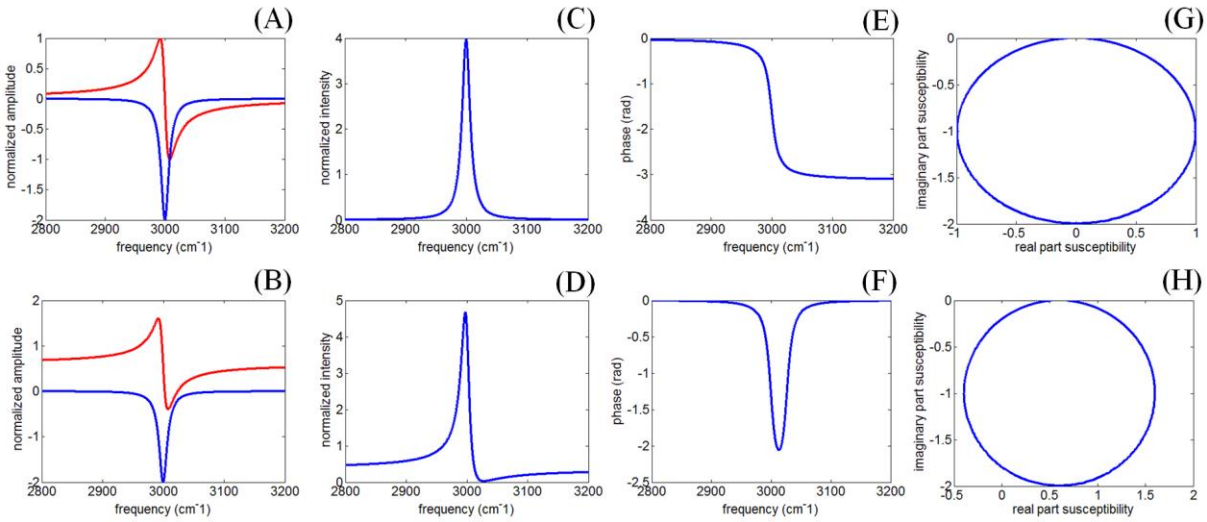

Figure 2.8: *Top: resonance without non-resonant background. Bottom: resonance with non-resonant background. (A and B) Real (red) and imaginary (blue) components of* $\chi_R^{(3)}$*. (C and D) Intensity of a single resonance* $\left|\chi_R^{(3)}\right|^2$*. (E and F) Phase response of a resonance. (G and H) imaginary vs. real component of* $\chi_R^{(3)}$*.*

2.5 Phase shaped broadband CARS

2.5.1 CARS excitation

The previous chapters showed how the CARS intensity is related to the molecules' third order susceptibility and how this susceptibility is related to the molecules' vibrational modes. With this knowledge we can use the expression for $\chi^{(3)}$ and the Raman spectrum of a compound to reconstruct the molecules' vibrational phase. The Raman spectrum is proportional to the imaginary part of $\chi^{(3)}$. Because the real and imaginary components are related to each other in a fixed way the Raman spectrum can be used to reconstruct the complete resonant part of $\chi^{(3)}$.

$$\chi^{(3)} = \sum_R \frac{A_R}{\omega_R^2 - \omega^2 + 2i\gamma_R\omega} + \chi_{NR}^{(3)} \qquad (2.7)$$

The information of the vibrational phase can be used to influence the generated CARS intensity. To observe a significant effect of the phase shaping, the excitation spectrum should have a bandwidth comparable to or exceeding the linewidth of a vibrational resonance, so that the vibrational phase varies substantially over the bandwidth of the laser pulse. In our system the pump and probe field are taken from the same laser source and have a broadband spectrum, and the shaping is done on the pulses of this laser. The Stokes laser has a very limited bandwidth and is used without any phase shaping.

To calculate the effect of an applied phase profile on the pump / probe pulse we use formula (2.2) describing the CARS intensity generated in our broadband setup. We use the complete amplitude and phase of $\chi^{(3)}$ and the applied shape on the broadband pump and probe field. The Stokes field is narrowband. When we calculate the convolution of the probe field with the susceptibility polarized by the pump and Stokes fields we find the effect of the applied shape on the CARS intensity. The convolution will result in the CARS field, where each frequency component consists of a sum of different resonances shifted to the same anti-Stokes frequency through the convolution with the broadband probe field. The sum of these resonances leads to constructive and/or destructive interference. By controlling the phase profile of the excitation laser fields we can influence this interference and the CARS intensity.

Our goal is to only optimize the intensity of the resonant contributions and discard the non-resonant background signal. For this reason we measure two CARS intensities; one obtained with a pulse with a positive phase shape $\phi(\omega)$ and one with a pulse with a negative phase shape $-\phi(\omega)$. The non-resonant background does not depend on the sign of the phase profile and as a result the background will be suppressed in the difference intensity. The reason that the background does not depend on the sign is that it has a flat phase response and is therefore insensitive to the direction of the applied phase response.

This subtraction scheme makes it possible to do measurements of a single compound in which the background signal is suppressed. As we can use shaping to get a larger or smaller CARS signal we can also apply shapes that have a zero or low difference CARS intensity for a specific compound. As such shaping can also be used to suppress the resonant signal of a compound. This has the potential to be used for the suppression of compound signals to get a better image of other compounds in the sample. In this situation the signal of one compound can be enhanced and the signal of the other compounds can be suppressed. As a result we can make a CARS intensity plot of the sample with an enhanced contrast for a compound of interest.

2.5.2 Covariance Matrix Adaptation Evolution Strategy

To obtain the optimal phase profile for selective excitation of a compound of interest we can take either a numerical or experimental approach. In both cases Covariance Matrix Adaptation Evolution Strategy (CMA-ES) is used. This is an evolutionary strategy that optimizes a set of parameters by maximizing a feedback parameter (fitness value). For a single compound we take the difference in CARS intensity between the positive $\phi(\omega)$ and negative $-\phi(\omega)$ shaped pulse as fitness.

$$F = \left| \int_{\omega_{min}}^{\omega_{max}} I_{CARS}\big(\phi(w)\big) - I_{CARS}\big(-\phi(w)\big) \cdot d\omega \right| = \Delta I_{CARS} \qquad (2.8)$$

The pump and probe phase profile is obtained by optimizing the phases of a set of points that are evenly spaced over the laser spectrum, and interpolating these results.

In the case that optimization for one compound is combined with suppression for the other compounds, a new fitness value is needed. Here the integrated difference CARS intensity of the compound of interest is taken and subtracted from this is the difference intensity from all other compounds multiplied with a constant α. This constant is empirically determined and chosen to obtain a maximized contrast for the compound of interest.

$$F = \Delta I_{compound\ of\ interest} - \alpha \sum \Delta I_{suppressed\ compounds} \qquad (2.9)$$

Thus the intensity of the compound of interest is optimized and the intensities of all other compounds are suppressed.

2.5.3 Compound mixture optimization

We have noted before that the CARS process depends on the modulus squared of the third order nonlinear susceptibility. Therefore a mixing term between the non-resonant background and the molecular resonances contributes to the CARS signal. This process in which a non-resonant term amplifies a resonant term is called homodyne mixing.

$$\left|\chi^{(3)}\right|^2 = \left|\chi_R^{(3)} + \chi_{NR}^{(3)}\right|^2 = \left|\chi_R^{(3)}\right|^2 + \left|\chi_{NR}^{(3)}\right|^2 + 2\chi_{NR}^{(3)} Re\left(\chi_R^{(3)}\right) \qquad (2.10)$$

In the same way another process can occur. When a broadband excitation laser is used multiple vibrational modes in a compound can be excited at the same time. Looking at formula (2.10) and

considering that the resonant term of the susceptibility is the sum of all vibrational modes one can see that a mixing term between these resonances will be present as well. An example in which 2 vibrational modes are excited is shown here:

$$\left|\chi^{(3)}\right|^2 = \left|\chi_{R1}^{(3)} + \chi_{R2}^{(3)}\right|^2 + 2\chi_{NR}^{(3)} Re\left(\chi_{R1}^{(3)} + \chi_{R2}^{(3)}\right) + \left|\chi_{NR}^{(3)}\right|^2 \qquad (2.11)$$
$$= \left|\chi_{R1}^{(3)}\right|^2 + \left|\chi_{R2}^{(3)}\right|^2 + 2 \cdot Re\left(\chi_{R1}^{(3)}\chi_{R2}^{(3)}\right) + 2\chi_{NR}^{(3)} Re\left(\chi_{R1}^{(3)} + \chi_{R2}^{(3)}\right) + \left|\chi_{NR}^{(3)}\right|^2$$

Here the resonant mixing term is $2 \cdot Re\left(\chi_{R1}^{(3)}\chi_{R2}^{(3)}\right)$. We can conclude that mixing occurs between resonances in a single compound, but when multiple compounds are present in the focal volume a CARS signal can also be generated through mixing between resonances of the different compounds. As different CARS signals are created for a mixture of compounds and the individual pure compounds, it might be possible to use phase shaping to selectively excite a mixture of compounds.

To verify that we obtain a signal from mixed compounds, a flow cell is used in which 2 pure liquids and their mixture are sent through 3 channels. A numerical evolutionary optimization can be performed to find a phase shape that enhances the signal of the mixture and suppresses the signal of the individual components. The fitness value for this optimization is chosen as:

$$F = \Delta\left|E_{compound1} + E_{compound2}\right|^2 - 2 \cdot \Delta\left|E_{compound1}\right|^2 - 2 \cdot \Delta\left|E_{compound2}\right|^2 \qquad (2.12)$$

3. Experimental CARS setup

3.1 Overview

In the CARS setup two 80 MHz repetition rate, mode locked lasers are used to generate the degenerate pump and probe field and the Stokes field. The lasers are synchronised and with the correct adjustment to the delay lines in both paths we ensure that the pulses of both lasers arrive at the same time at the sample. The synchronisation will be further explained in chapter 3.2. The Ti:Sapphire laser generates broadband pulses with a center wavelength around 800 nm and average power of 230 mW that are used for the pump and probe field. By splitting off power for synchronisation and losses in the shaper setup this average power drops to 27 mW before reaching the sample. The Nd:YVO_4 laser has an average output power of 2.18 W and generates narrowband picosecond pulses for the Stokes field. This power drops to 120 mW before reaching the sample, mainly due to spatial filtering, modulation with an AOM and a beamsplitter for laser synchronisation. 15% of the intensity from the Nd:YVO_4 laser and 25% from the Ti:Sapphire laser is used for optical synchronisation. The rest of the light from the Nd:YVO_4 laser is sent through a delay line for temporal overlap with the Ti:Sapphire at the sample. The light from the Ti:Sapphire that is not used for synchronisation is sent to the shaper where a phase profile can be applied to the spectrum. (Further details are presented in chapter 3.3). Both beams are aligned into the microscope and the CARS signal from the sample is detected using a silicon photodiode. A short-pass filter (Thorlabs FM-01) is placed after the microscope to reflect most of the 800 nm and 1064 nm light into a second silicon photodiode. The signal from this second photodiode is used to measure the transmission of light through the sample. When CARS measurements are done on liquids, a flow cell is placed between the microscope objectives. The flow cell or other samples are mounted on a XZ-scanning stage with a scan range of approximately 320 by 320 µm, replacing a previous scanning stage that could not lift the flow cell's weight and had a range of only 80 by 80 µm. Figure 3.1 shows a simplified schematic of the setup. A more extensive overview of the setup can be found in appendix C.

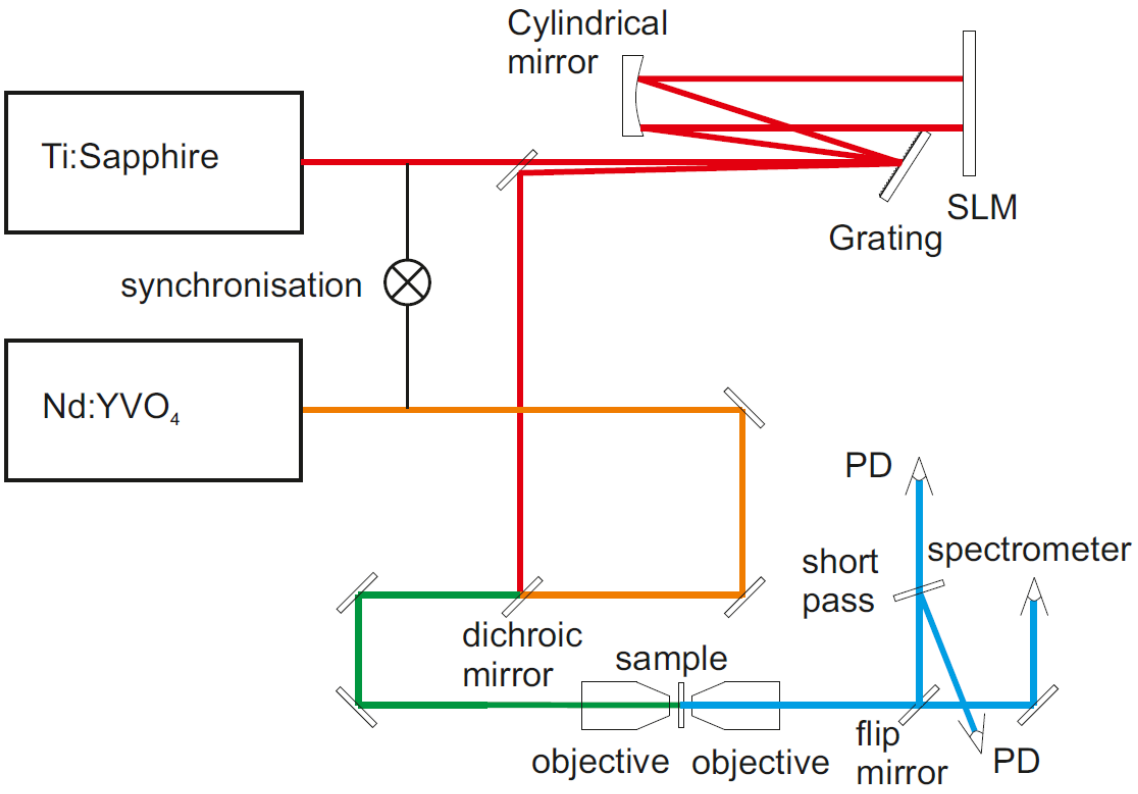

Figure 3.1: *Schematic overview of the CARS setup.*

For microscopic imaging, a 0.6 numerical aperture (NA) Nachet Plan Fluor 40x near-infrared air objective is used as the illumination objective. This objective is mounted on a XYZ- translation stage (Newport Ultra align, model 5610). The collection objective is a 0.5 NA extra-long working distance Nikon M-Plan 40x air objective. The collection objective is mounted on a Melles Griot XYZ-translation stage.

The CARS signal is measured with a silicon photodiode measured or spectrally resolved using a spectrometer (Avantes AvaSpec 3648 USB2). The transmission of the Ti:Sapphire light through the sample is measured on another silicon photodiode, using a short-pass filter (Thorlabs FM-01) in the beam path to separate the 800 nm and 1064 nm light from the CARS signal. To separate the CARS signal from the excitation light, a filterset containing the following filters is used: 2x Chroma HQ 655/50 M-2P, 2x Thorlabs FB650-40, 1x Thorlabs SP700, 1x Thorlabs FM01. The filterset for transmission measurements in front of the second photodiode contains the following filters: 2x Thorlabs FB800-40, 1x Thorlabs SP1000.

For the scanning of the sample in the microscope, first a XZ-piezo scanner of Piezosystem Jena was used, with a scanning range of approximately 80 by 80 μm. For the CARS measurements on liquids, a different stage containing 2 piezo actuators was used. This scanner contains separate piezo actuators for the x (PX 400 SG) and the z direction. Both actuators have a range of 400 μm in open loop and 320 μm in closed loop operation.

The CARS signal is detected using a lock-in amplifier and an acousto-optic modulator (AOM). The AOM modulates the Stokes beam and the CARS signal is detected at this modulation frequency using an EG&G Princeton Applied Research Model 5210 lock-in amplifier. The AOM is an Isomet M1080 T90L is powered by an Isomet model 532C-4 driver. The modulation on the Stokes beam is applied with a Hameb HM8030-4 function generator.

3.2 Laser synchronisation

To ensure that the pulses of both lasers arrive at the sample simultaneously, it is necessary to synchronize the repetition rate of both lasers. In our system the Ti:Sapphire laser is synchronised to the Nd:YVO_4 laser. The synchronisation process is done in several steps. The pulse trains of both lasers are detected using two ultrafast photodiodes. For the Ti:Sapphire laser a silicon photodiode is used, and for the Nd:YVO_4 laser an InGaAs photodiode is used. The photodiode signals are filtered with a 90 MHz low pass filter. Through mixing of these signals, the difference frequency in repetition rate from the two lasers is obtained. By controlling a motorized translation stage that is attached to the output coupler in the Ti:Sapphire cavity, the cavity length can be changed. This allows us to manually regulate the repetition rate of the Ti:Sapphire laser. We use this manual control to bring the difference frequency between the two lasers within several Hz. Next, a feedback loop for electronic synchronisation is used. This feedback loop controls two piezo actuators, one on the high reflector and one on the output coupler of the Ti:Sapphire cavity. The piezo on the high reflector is used for slow control of the repetition rate, reacting to fluctuations below 3 Hz, while the piezo on the output coupler is used for fast control of the repetition rate at frequencies above 3 Hz.

A patch cable box in the Ti:Sapphire signal branch can be used to provide an electronic delay to the photodiode signal of this pulse train. The delay that can be provided with this box is up to 127.5 ns, with a 500 ps stepsize. In the signal branch of both lasers there is a tuneable band-pass filter that is used to make fine adjustments in the delay of either laser's pulse train. With the electronic locking the pulse trains are synchronised, however there are some fluctuations in the delay between the pulses. Therefore a more sensitive feedback loop is necessary and this is done with optical synchronisation.

For optical synchronisation, a part of the Ti:Sapphire and Nd:YVO_4 laser beams is split of using a pellicle beamsplitter for the Ti:Sapphire and a half-wave plate and polarizing beamsplitter for the Nd:YVO_4. These split off beams are combined with a dichroic mirror and focused in a Barium borate (BBO) crystal. In this crystal a sum frequency generation (SFG) process occurs. The SFG signal is

detected on a silicon photodiode and is used as a feedback parameter. A filterset is placed in front of the photodiode to remove the excitation light of both lasers and SHG light of the 800 nm and 1064 nm created in the BBO crystal. The filterset contains the filters: 2X Thorlabs FB 450-40 and 1X Thorlabs FES0700. When the SFG is used in the feedback loop the timing drift can be greatly reduced.

3.3 Shaper

The phase shaping setup consists of an 830 lines per mm grating, a folding mirror, a cylindrical mirror with a focal length of 593 mm and a spatial light modulator (SLM). The incoming light is diffracted from the grating and focused with the cylindrical mirror on a 640 pixels liquid crystal based SLM. For a schematic representation of the shaper setup see Figure 3.2 (A). The light travels through the SLM and is reflected from a mirror mounted on the backside of the SLM. The beam is reflected back along almost the same path and comes out of the shaper setup with a slight vertical offset compared to the incoming beam, so that the beams can be separated. The SLM and folding mirror are both mounted on a translation stage so that they can be placed exactly in the focus of the cylindrical mirror. Phase modulation is applied on the spectrum when the pulses travel through the SLM. The SLM is operated by applying a voltage to the individual pixels. The liquid crystals provide an electrically variable polarization rotation of the light which influences the refractive index from the liquid crystal. This refractive index change is used to control the applied phase on the light as the light travels through the medium. The SLM can also be used for amplitude modulation. For this an input and output polarizer are used with the liquid crystal's (LC) extraordinary axis under an angle of 45° with respect to the polarizers. Now the LC mask functions as an electrically variable waveplate and the output polarizer modifies the amplitude. In our system the SLM contains two masks which allows for individual phase and amplitude shaping. By aligning the masks orthogonally to each other the phase modulation is proportional to the sum of the modulation in both masks and the amplitude modulation is proportional to the difference in modulation in both masks. A schematic representation of the SLM is shown in Figure 3.2 (B).

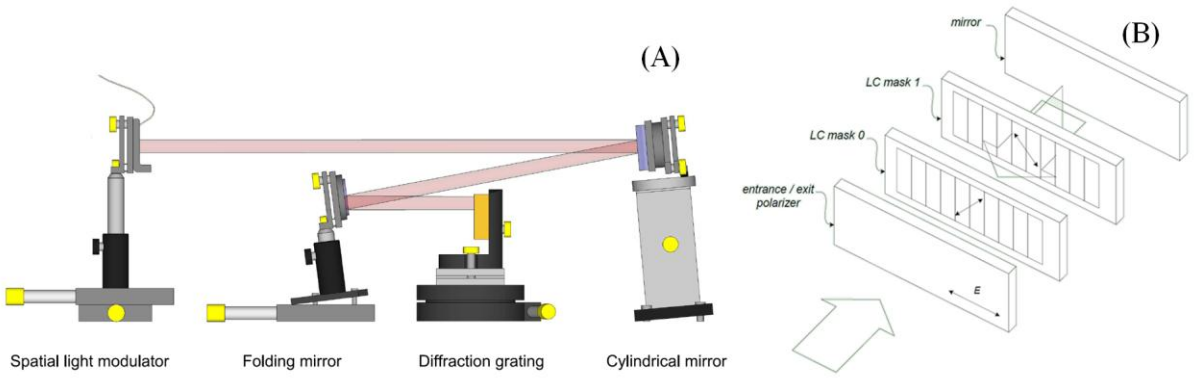

Figure 3.2: *(A) Schematic overview of the shaper*[26]*. (B) SLM components*[27]*.*

The intensity modulation at the exit polarizer is proportional to the cosine of the total polarization change in the SLM.

$$\Delta I \propto cos(\Delta P_{mask1} + \Delta P_{mask2}) \qquad (3.13)$$

Since the SLM is operated in phase only shaping mode it is necessary to keep $\Delta P_{mask1} = -\Delta P_{mask2}$ so that ΔI will be kept at 1. Phase modulation is obtained by the change in refractive index for light with a rotated polarization. The polarization is changed in the first mask to obtain a new effective refractive index and the second mask is used to rotate this polarization back to its original state. The phase change is thus proportional to half of the difference in polarization rotation in the masks.

$$\Delta\varphi \propto \frac{\Delta P_{mask1} - \Delta P_{mask2}}{2} \tag{3.14}$$

Because the LC masks are aligned orthogonally to each other the same drive levels can be applied to obtain an inverse polarization rotation in mask 1 and 2. This results for the phase modulation in:

$$\Delta\varphi \propto \frac{\Delta D_{mask1} + \Delta D_{mask2}}{2} \tag{3.15}$$

Here ΔD_{mask1} and ΔD_{mask2} are the drive levels in radians in mask 1 and 2 respectively. $\Delta\varphi$ represents the phase modulation in radians applied by the SLM. Considering the orthogonal alignment of the LC masks the relation for amplitude modulation is:

$$\Delta I \propto cos^2\left(\frac{1}{2}(\Delta D_{mask1} - \Delta D_{mask2})\right) = \frac{1 + cos(\Delta D_{mask1} - \Delta D_{mask2})}{2} \tag{3.16}$$

Here ΔD_{mask1} and ΔD_{mask2} describe the drive levels of mask 1 and 2 in radians. ΔI Describes the intensity modulation, where $\Delta I = 1$ means no modulation and $\Delta I = 0$ means maximum modulation.

3.4 Flow cell

In order to obtain CARS measurements on liquids, a flow cell has been implemented in the setup. The flow cells were obtained from Micronit microfluidics and have channel widths ranging from 10 to 100 µm with a channel depth of 20 µm. The cells are placed in a connectorized casing and attached to the scanner stage. The liquids are pumped into the channels from HAMILTON syringes with a syringe pump (Chemix Inc. Model: Fusion 400).

Two different flow cells have been used in this work. Both have different channel widths and a different layout of the channels as is shown in Figure 3.3 (A and B). The first cell (figure A) contains five individual channels that are aligned parallel to each other. All five channels have a width of 10 µm and are separated by a distance of 30 µm from each other. This flow cell can be used to image the signal obtained from five separate components. The second cell (figure B) consists of two sets of 3 channels with 30 µm width that combine into a single channel of 80 µm width. It also contains a single channel running over the length of the cell. The combining channels can be used to image the CARS signal of multi-compound mixtures.

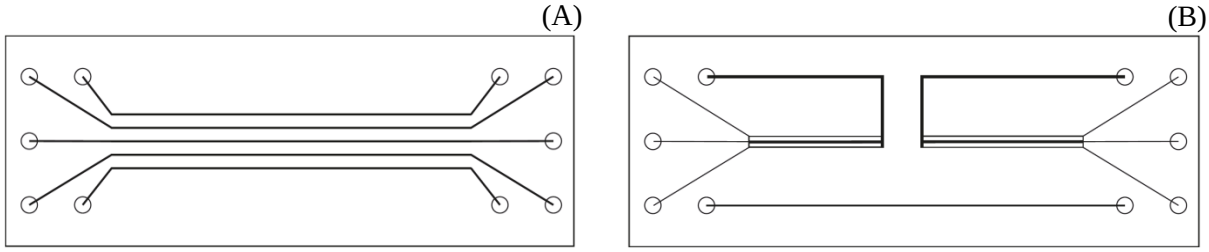

Figure 3.3: *The two flow cells for measurements on liquids.(A) contains five parallel channels. (B) contains two sets of mixing channels.*

4. Phase shaped CARS

4.1 Numerical evolutionary optimization

The evolutionary optimization can be performed numerically. This allows us to calculate an optimum phase profile before doing an experiment. Numerical simulations are also used to investigate the possibility to optimize the CARS response of a mixture of compounds and the effectiveness of this optimization.

The simulations require the molecular response function or nonlinear susceptibility. The nonlinear susceptibility is approximated with a sum of damped harmonic oscillators and a non-resonant background. The susceptibility can be modelled using the spontaneous Raman spectrum of the compound. The Raman spectrum intensity is proportional to the imaginary part of the susceptibility[28].

$$I_{Raman}(\omega) \propto Im\left(\chi^3(\omega)\right) = A\left(\chi^3(\omega)\right) \cdot sin\left(\varphi\left(\chi^3(\omega)\right)\right) \tag{4.17}$$

Since the imaginary part is related to the real part in a fixed way we can use this to reconstruct the total nonlinear susceptibility. This is done by fitting the Raman spectrum to the imaginary part of a sum of vibrational resonances. As each vibrational resonance is described as a damped harmonic oscillator, we need to find a sum of oscillators of which the imaginary part fits the Raman spectrum.

$$\chi_R^{(3)} = \sum_R \frac{A_R}{\omega_R^2 - \omega^2 + 2i\gamma_R\omega} \tag{4.18}$$

We use CMA-ES to fit the imaginary part of the sum of these resonances to the Raman spectrum. The amplitude, width and resonance frequency of each resonance are taken as optimization parameters. Typically 30 to 50 resonances are modelled. As fitness we use the negative of the mean squared error between the complex part of the fitted function and the Raman spectrum.

$$F = -\frac{1}{N}\sum_{\omega=\omega_{min}}^{\omega_{max}} \left(Im\left(\chi^3(\omega)\right) - I_{Raman}(\omega)\right)^2 \tag{4.19}$$

The result of this process is that all vibrational modes are modelled, but we do not obtain the non-resonant background. Because the non-resonant background has no imaginary component it does not show up in the Raman spectrum and cannot be retrieved in the evolutionary optimization. The non resonant background can be added to the obtained fit as a constant value or a slowly varying frequency dependent function. In our simulations, we use a constant value of 20% of the amplitude of the highest vibrational mode peak. This is an empirical value that was found to be in reasonable agreement with experimental results.

4.2 Compound optimization

We consider a test-case of a mixture of toluene and ethanol and perform two separate numerical optimizations; one for selective excitation of toluene while suppressing ethanol and one for selective excitation of ethanol while suppressing toluene. For these optimizations we use the Raman spectrum of the two components to model their nonlinear susceptibility The pump and probe excitation field has a center wavelength of 809 nm and a full width at half maximum (FWHM) of 13.1 nm. Figure 4.1 shows the Raman spectra of both compounds and the normalized excitation pump field. The amplitudes of the Raman spectra are normalized to the peak value of the ethanol spectrum.

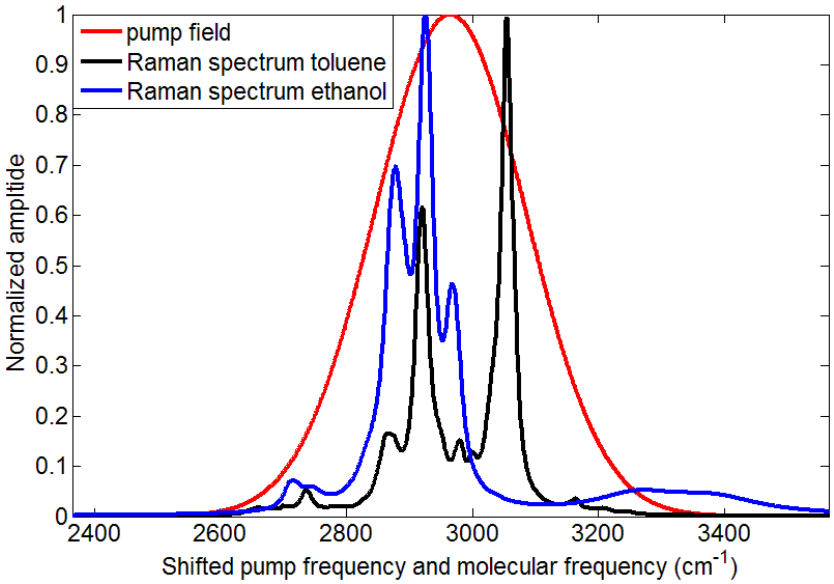

Figure 4.1: *Normalized amplitude of the pump field (red), Raman spectrum of toluene (black) and ethanol (blue)*

From the Raman spectrum the complete complex vibrational response of the molecule is modeled as described in chapter 4.1. With the vibrational response we can calculate the intensity of the CARS signal and the optimal phase profiles for selective excitation. The amplitude and phase of the response can be seen in Figure 4.2 A and B respectively. The amplitude of both toluene and ethanol are normalized with respect to the maximum amplitude of ethanol.

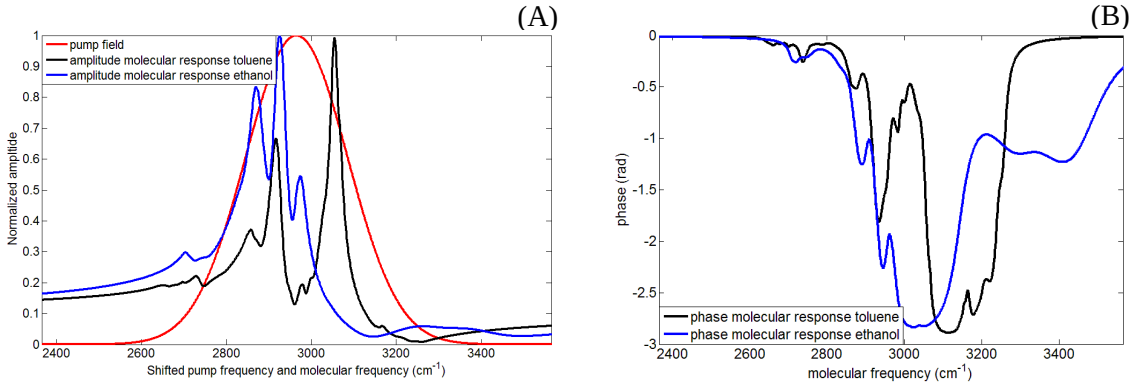

Figure 4.2: *(A) Normalized amplitude of the pump field (red), amplitude molecular response of toluene (black) and ethanol (blue). (B) Phase molecular response of toluene (black) and ethanol (blue)*

We run the optimization for selective excitation of either compound based on the compounds' vibrational response functions. Here the difference intensity of the compound of interest is maximized and the difference intensity of the other compound is minimized. This has been done for both compounds and the two excitation phase profiles are shown in Figure 4.4 A and B respectively. We use the CMA-ES program as explained in 2.5.2. The obtained fitness value for each generation is shown in Figure 4.3.

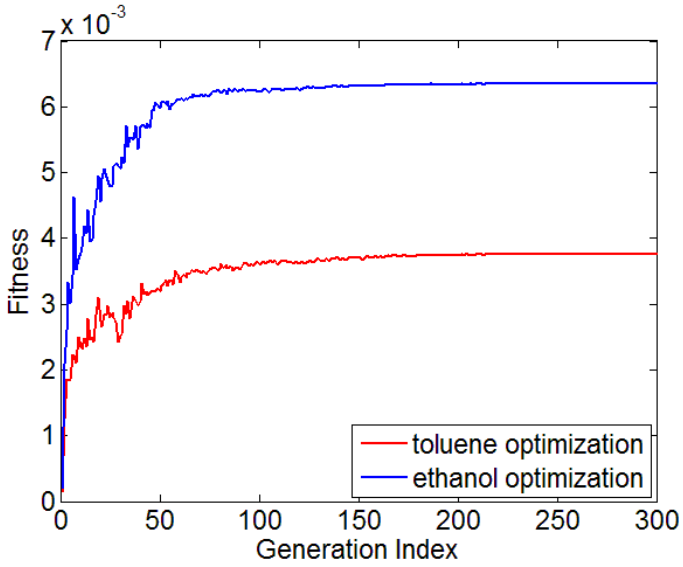

Figure 4.3: *Obtained fitness during optimization process. Fitness for toluene optimization (red) Fitness for ethanol optimization (blue)*

We can see that the program quickly converges to an optimum. From the amplitude of the molecular response we have seen that at these concentrations the total signal is larger for ethanol. As a result the obtained maximum fitness value is also higher when optimizing for ethanol.

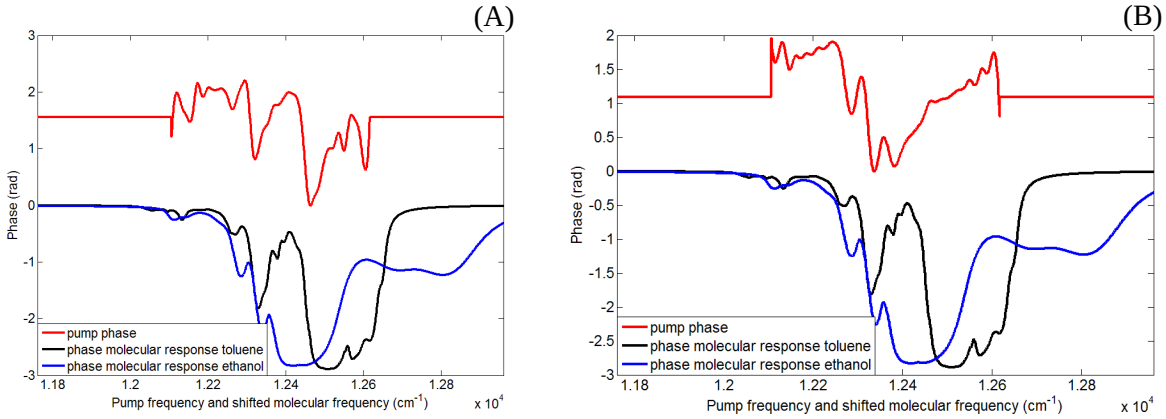

Figure 4.4: *(A) Phase profile for selective excitation of toluene and suppression of ethanol (red), phase molecular response toluene (black) and ethanol (blue). (B) Phase profile for selective excitation of ethanol and suppression of toluene (red), phase molecular response toluene (black) and ethanol (blue)*

Figure 4.4 A and B show the excitation phase for the optimization of toluene and ethanol respectively. We can achieve an enhanced contrast with this optimization. The contrast $\frac{I_{CARS\ compound1}}{I_{CARS\ compound2}}$ obtained when the optimization converges to an optimum is 1100 for toluene and 1200 for ethanol.

4.3 Mixture optimization

We have also investigated the possibility to optimize a mixture of components. As a proof of principle we use the feedback loop to numerically optimize the response of a 50/50 mixture of toluene and ethanol, while the signal of the pure components of toluene and ethanol are suppressed. The complex vibrational response is obtained from the spontaneous Raman spectra, as shown in Figure 4.2. The

fitness values during the optimization can be seen in Figure 4.5. Each generation consists of 40 individuals and the best and worst values per generation are shown. The fitness values are defined as:

$$F = \Delta|E_{ethanol} + E_{toluene}|^2 - 2|E_{ethanol}|^2 - 2|E_{toluene}|^2 \qquad (4.20)$$

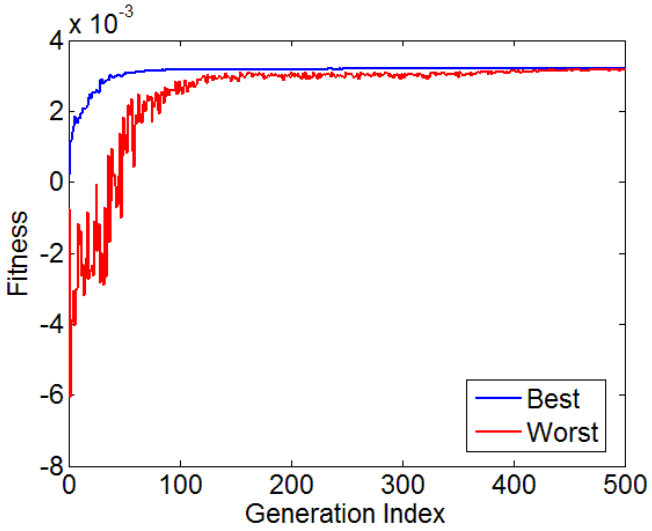

Figure 4.5: *Best (blue) and worst (red) fitness per generation*

We can see that the optimization converges to an optimum. The result of the optimization is the excitation phase profile, shown together with the molecular phase of the compounds in Figure 4.6. It appears that even though this optimization is more complex compared to the optimization of selective excitation of a pure compound, the number of generations it takes to reach an optimum value does not significantly increase.

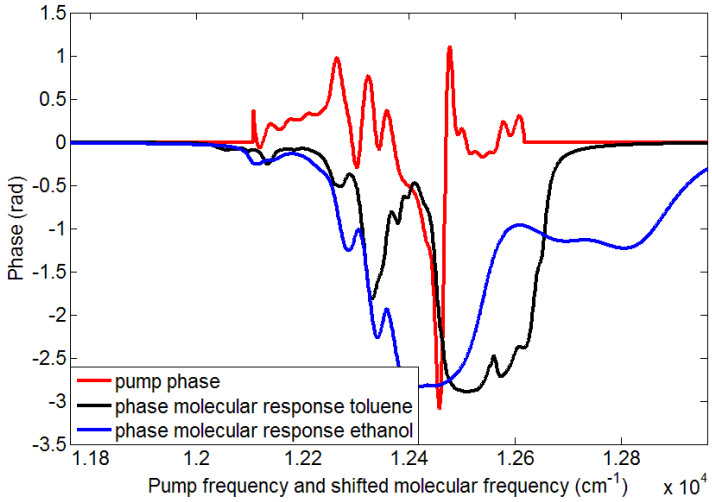

Figure 4.6: *Excitation phase profile (red). And the phase of the molecular response of toluene (black) and ethanol (blue).*

The obtained contrast is defined as $\frac{I_{CARS\ compound\ mixture}}{\max(I_{CARS\ compound1}, I_{CARS\ compound2})}$. The contrast obtained with the program is 16. Because there is more overlap in the compounds molecular phases the optimization becomes more complex, it is thus to be expected that the obtained contrast is lower.

5. CARS imaging

As we have simulated in chapter 4 we are able to use spectral shaping to influence the CARS signal of specific compounds. This allows us to create CARS images where the non-resonant background is removed and where the intensity of compounds can be enhanced or suppressed for an enhanced contrast. In this chapter we show selective imaging with background removal of plastic beads and liquids.

5.1 Compound optimization

Figure 5.1 shows the result from an experimental optimization experiment for background suppression on 20 µm Poly(methyl methacrylate) (PMMA) beads. The pump probe excitation field has a center wavelength of 803 nm with a 16 nm FWHM. We show CARS intensity plots created with unshaped excitation pulses, shaped pulses with the phase profile shown in Figure 5.1 (E), shaped pulses with the negative of this phase profile and an image of the difference intensity between the images created with the positive and negative shaped pulses. We see an increase in contrast in the signal obtained from the PMMA vs. the signal of the water. With $\text{contrast} = \frac{|I_{PMMA}|}{|I_{water}|}$ the intensity plot with unshaped excitation light shows a contrast of 1.2 and the difference intensity image shows a contrast of 4.8.

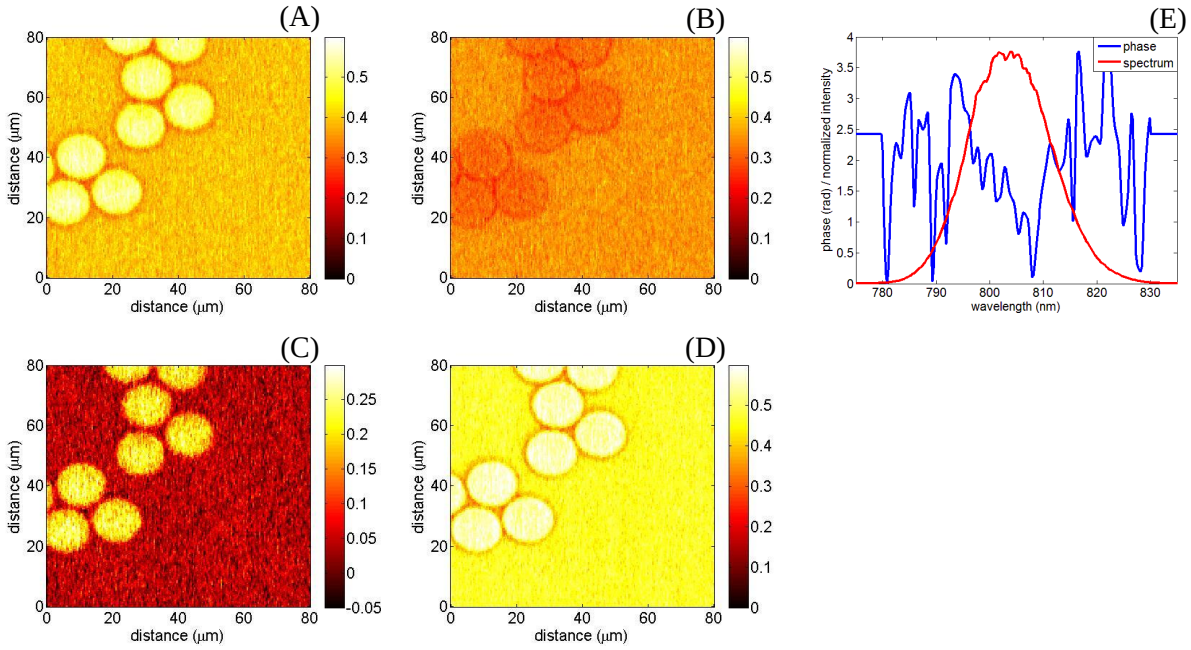

Figure 5.1: *(A) Intensity image created with the positive excitation phase. (B) Intensity image created with the negative excitation phase. (C) Difference intensity image of figure A and B. (D) Intensity image created with unshaped excitation pulses. (E) Applied pump / probe spectrum with phase profile.*

Figure 5.2 and Figure 5.3 both show selective excitation of Polystyrene (PS) beads with suppression of PMMA beads and non-resonant background. Both figures show images of the transmitted light intensity, the CARS signal with unshaped excitation pulses, the CARS signals with positive and negative shaped excitation pulses, the difference intensity of the images created with the positive and negative shaped pulses and the spectrum of the pump / probe field with the applied phase profile. The contrast that we obtain is defined as $\frac{|I_{PS}|}{max(|I_{PMMA}|,|I_{water}|)}$ for Figure 5.2 this is with an unshaped excitation pulse 2.0 when taking the difference intensity obtained from the positive and negative shaped pulses this is increased to 4.5. For Figure 5.3 the obtained contrast is increased from 2.1 to 6.5. For the measurement shown in Figure 5.3 a different scanning stage was used this has allowed us to increase the scanning range from 80 X 80 µm to 320 X 320 µm. As this is a 16 times larger scanning

range we have been forced to decrease our resolution and integration time to keep the measurement time within one hour per image.

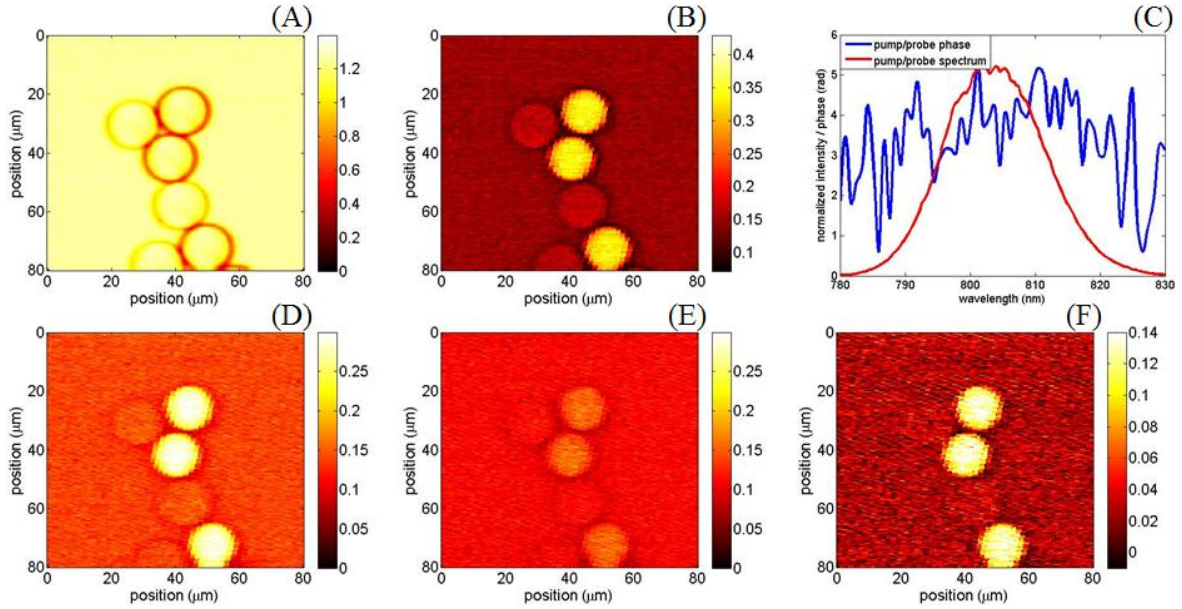

Figure 5.2: *(A) Intensity plot of transmitted excitation light. (B) Intensity plot created with unshaped excitation pulses. (C) Applied pump and probe spectrum with phase profile. (D) Intensity plot created with positive shaped excitation pulses. (E) Intensity plot created with negative shaped excitation pulses. (F) Intensity difference plot of image D and E.*

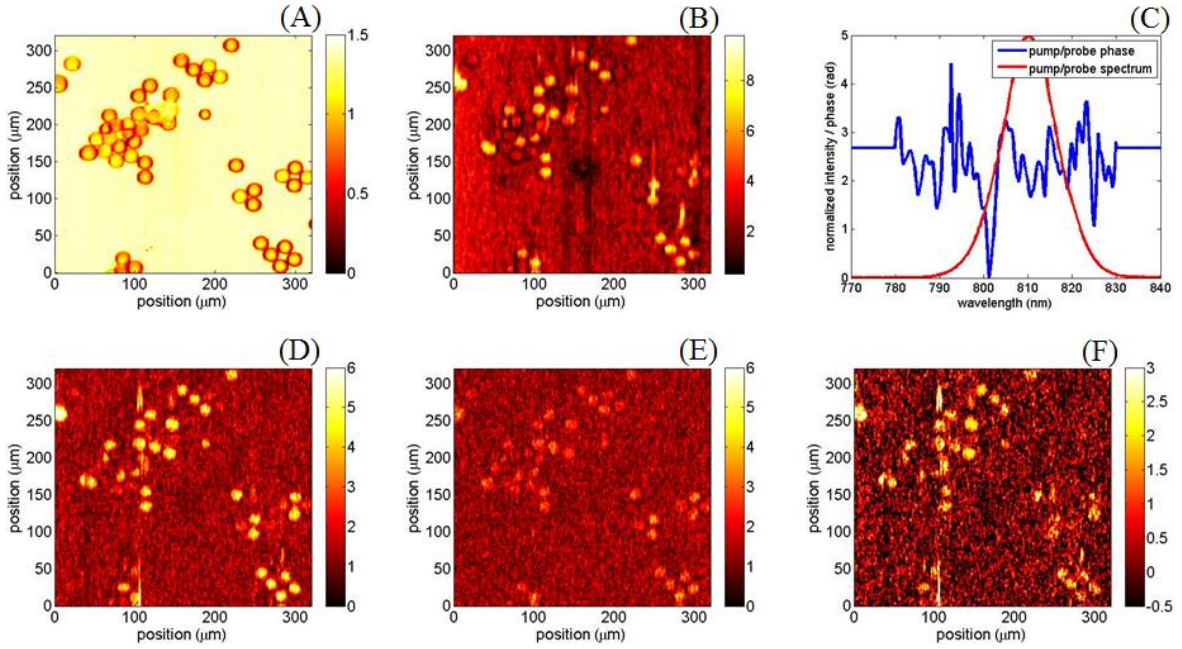

Figure 5.3: *(A) Intensity plot of transmitted excitation light. (B) Intensity plot created with unshaped excitation pulses. (C) Applied pump and probe spectrum with phase profile. (D) Intensity plot created with positive shaped excitation pulses. (E) Intensity plot created with negative shaped excitation pulses. (F) Intensity difference plot of image D and E.*

5.2 Liquids imaging

We have performed CARS imaging on liquids in a flow cell. Figure 5.4 shows the signal of acetone measured over three parallel channels excited with unshaped excitation pulses. From figure (A) we see that the signal is low in comparison with the plastic beads of earlier experiments, therefore we have chosen to apply a 3 X 3 moving window average. To obtain a better visibility we show a second figure (B) where we have averaged the CARS signal over the horizontal axis of figure (A).

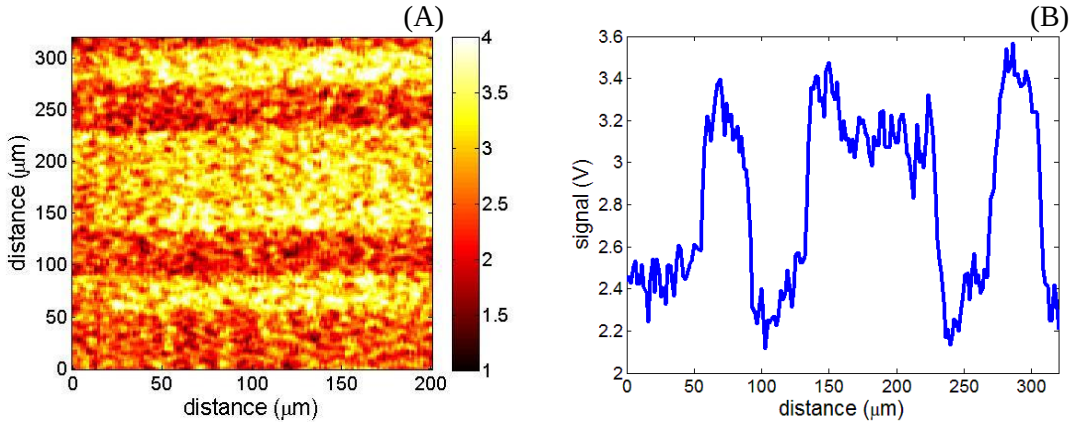

Figure 5.4: *(A) Intensity plot of CARS signal. (B) CARS signal averaged along the horizontal axis of figure A.*

Figure 5.5 shows selective excitation of ethanol with non-resonant background suppression. Figure (A) shows the signal excited with positive shaped excitation pulses, figure (B) is created with negative shaped excitation pulses, figure (C) shows the difference signal of figure A and B, and figure (D) shows the signal excited with unshaped excitation pulses. The used pump and probe spectrum with excitation phase is shown in figure (E). It should be noted that the low intensity spots, obtained in the measurement performed with positive shaped pulses, are due to air bubbles propagating through the channel and are as such not a contribution of ethanol. We can report an enhancement in contrast $\frac{|I_{ethanol}|}{|I_{glass}|}$ from 1.3 with unshaped imaging to 3.8 for the difference intensity image.

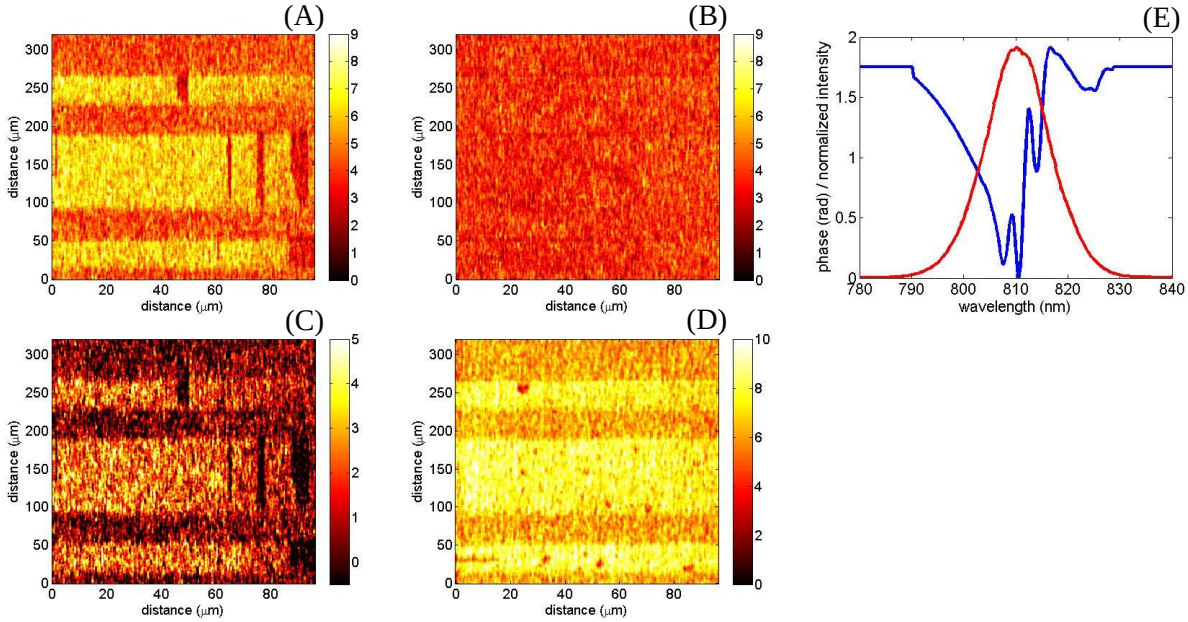

Figure 5.5: *(A) Intensity excited with positive shaped pulses. (B) Intensity excited with negative shaped pulses. (C) Difference intensity of figure A and B. (D) Intensity excited with unshaped pulses. (E) Pump and probe intensity spectrum and applied phase profile.*

In Figure 5.6 we show selective excitation of ethanol with suppression of toluene. Figure (A) shows the signal excited with positive shaped excitation pulses, figure (B) is created with negative shaped excitation pulses, figure (C) shows the difference signal of figure A and B, and figure (D) shows the signal excited with unshaped excitation pulses. The used pump and probe spectrum with excitation phase is shown in figure (E). Just as in the experiment performed on acetone (Figure 5.4 (B)) we show the averaged signal along the vertical direction. The measurement is performed along three channels. The first channel centered between 20 µm and 50 µm contains toluene, the third channel centered between 230 µm and 260 µm contains ethanol. These two channels have been combined into the second channel centered between 100 µm and 180 µm, as such this contains a mixture of ethanol and toluene. We see that in the difference intensity image that most of the resonant contribution of ethanol is preserved while other signals are suppressed. It can also be seen that the background is not completely suppressed, this is most likely a result of remaining chirp on the unshaped excitation pulses.

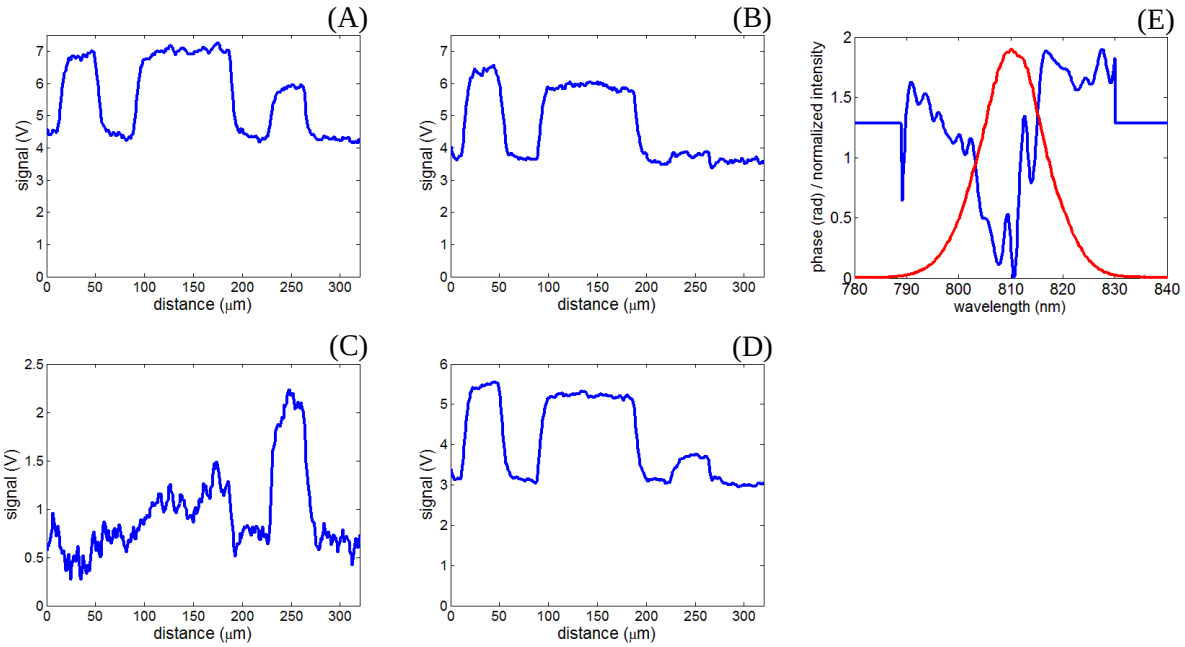

Figure 5.6: *(A) Intensity excited with positive shaped pulses. (B) Intensity excited with negative shaped pulses. (C) Difference intensity of figure A and B. (D) Intensity excited with unshaped pulses. (E) Pump and probe intensity spectrum and applied phase profile.*

5.3 Discussion

In this chapter we have shown that we can use spectral shaping to influence the CARS intensity of individual compounds. We are able to remove the non-resonant background from our signal by taking the difference intensity between the signal obtained from positive and negative shaped pulses. Images have been obtained where contrast for specific compounds has been enhanced. CARS microscopy images are obtained from samples containing plastic beads and flow cells containing several liquids. The phase profiles used for these measurements have been obtained numerically or experimentally analogous to the numerical method described in chapter 4.

In many of the images the obtained contrast is lower than was expected based on simulations. This is mainly a result of noise on the CARS signal. There are several sources for this noise like small changes in alignment during the experiment, there is noise in the electronics and detector but the most noise is caused by intensity fluctuations in the Ti:Sapphire laser intensity. There are low frequency intensity fluctuations with an amplitude 2% to 3% of the laser intensity. Because the CARS signal is proportional to the square of this intensity this noise increases up to 6% in the signal. As we use the difference intensity of two images the noise again increases as the resulting image obtains the noise

from both measurements. Considering this the experiments can be greatly improved with a more stable pump / probe laser.

We have also seen that there are some differences between the phase profiles that have been obtained in a numerical or experimental optimization process. It has not been investigated what exactly causes these differences but there are several contributions that will certainly have an influence. In a numerical optimization we assume that the pump / probe pulses are transform limited where in reality due to imperfections in the shaper alignment and dispersive elements in the setup there will be some chirp on the excitation pulses. Furthermore there can be some errors in the shaper calibration which cause differences between the applied and calculated phase profiles. As a result of these differences a phase profile obtained in an experimental feedback often provides better images compared to a numerically obtained phase profile. This occurs because the CMA evolutionary strategy will converge to a solution while these imperfections are present and are thus incorporated in the solution.

With the ability to enhance contrast for specific compounds we have shown the proof of principle for a tool providing label free imaging that can be used for biological samples and medical imaging. The use of a flow cell provides a tool for influencing the CARS signal of liquids. This will allow us to optimize for mixing of multiple resonant compounds in a focal volume, which can be used to test more complex phase profiles for the simultaneous detection of multiple compounds in a single focal volume.

6. Chemical specificity by dispersion compensation

6.1 Dispersion compensation

Dispersion is a fundamental concept in optics in which the phase velocity of a light wave depends on its frequency as it propagates through a dispersive medium. Dispersion produces effects such as the separation of wavelengths in a prism and chromatic aberration in lenses. Another effect of dispersion is the temporal broadening of femtosecond pulses. In this situation the individual waves, that would constructively interfere for an ultrashort pulse, are shifted in phase and will result in a pulse with a longer time duration and lower peak intensity. Dispersion is therefore mostly an unwanted phenomenon in optics when dealing with ultrashort pulses[29].

In nonlinear and ultrafast optics, generally reflective optical elements are used rather than transmissive elements as these give a lot less or no dispersion. Furthermore it is often necessary to compensate the effects of dispersion. Dispersion can be compensated by using an SLM phase shaping setup[30] and applying the inverse phase profile of the dispersion to the spectrum of the light. Another method to compress pulses is by using a prism or grating compressor[31][32].

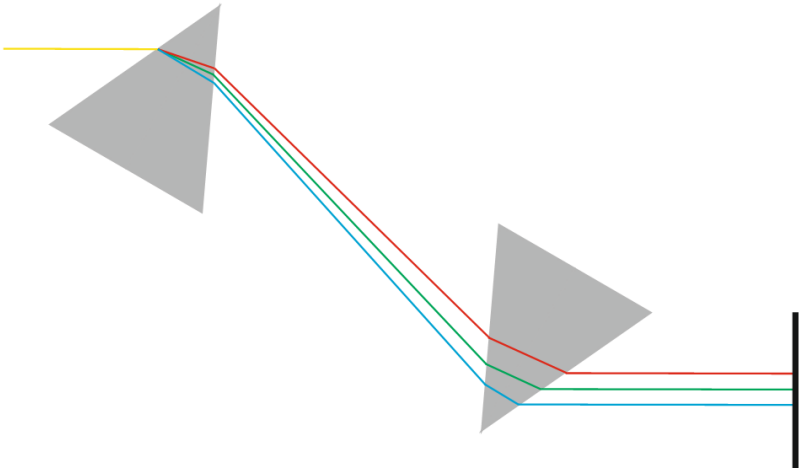

Figure 6.1: *Prism compressor*

For precise compensation it is necessary to monitor the amount of dispersion in the pulse after the compression. This can be done carefully by using an autocorrelator or frequency resolved optical gating (FROG) system, but it is generally easier to only detect the two photon signal[33]. This signal scales with the intensity squared of the excitation field and with more dispersion the peak intensity of the pulse will drop. It is therefore possible to adjust the dispersion compensation system for a maximized two photon signal. In our setup the two photon signal is created by second harmonic generation in a BiB_3O_6 crystal.

6.2 Dispersion of sharp resonances

The dispersion and absorption of a compound can both be obtained from the linear susceptibility χ of the compound. The dispersion is proportional to the real part of the complex susceptibility and the absorption is proportional to the imaginary part of the complex susceptibility. For most materials the dispersion is a result of broad electronic resonances and can be approximated by using the Sellmeier equations.

There is however also dispersion induced by narrowband electronic resonances. These resonances cause sharp absorption peaks and can cause a complex dispersion profile. In the case of these sharp resonances, the molecules susceptibility can be described by damped harmonic oscillators. These resonances can be described as oscillations of the electron cloud induced by the electric field of the light. The oscillation increases on frequencies close to a resonance frequency of the molecule. These

resonances can be described by damped harmonic oscillators. A single resonance is described in the following formula[34]:

$$\chi = \frac{Ne^2}{\varepsilon_0 \omega m_e} \frac{1}{\omega_0^2 - \omega^2 - i\gamma\omega} \tag{6.21}$$

We use the slowly varying envelope approximation to obtain the refractive index and absorption coefficient. The slowly varying envelope approximation gives[34]:

$$E_0(z) = E_0(0) e^{\left(i\frac{k}{2}\chi z\right)} \tag{6.22}$$

As χ is complex-valued we can see that the exponential will result in a phase and loss term. By defining separate quantities for the real and imaginary part we obtain:

$$\alpha = kIm(\chi) \tag{6.23}$$

$$(n-1)k = \frac{k}{2} Re(\chi) \tag{6.24}$$

$$E_0(z) = E_0(0) e^{i\left(i\frac{\alpha}{2}z + (n-1)kz\right)} = E_0(0) e^{-\frac{\alpha}{2}z} e^{i(n-1)kz} \tag{6.25}$$

The phase term described with the refractive index n is proportional to the real part of the susceptibility and the absorption described by the absorption coefficient α is proportional to the imaginary part of the susceptibility. From the equation for a single resonance we see that the dispersion and absorption are much more pronounced close to a resonance. This can also be seen in Figure 6.2.

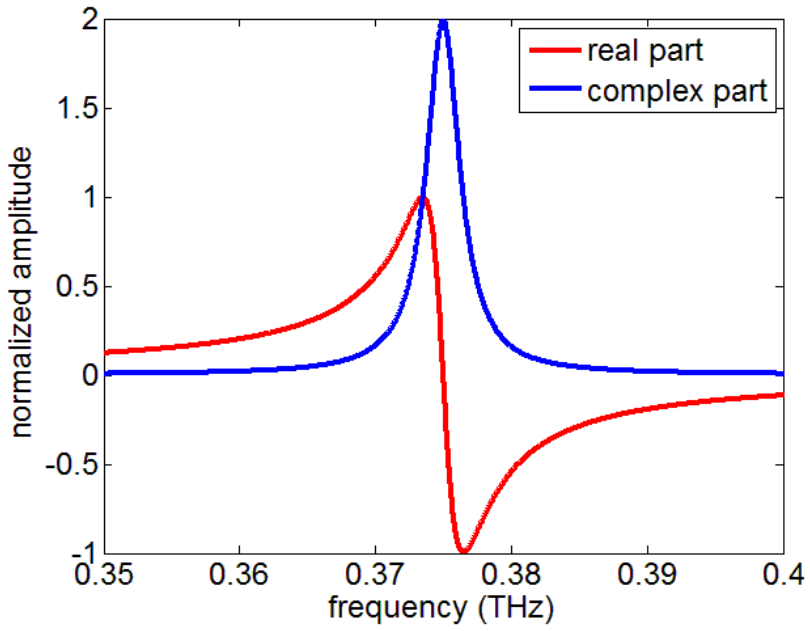

Figure 6.2: *The normalized real (red) and imaginary (blue) part of the susceptibility of a single harmonic oscillator.*

6.3 Modeling the dispersion profile

We have developed a procedure to calculate the phase change the light undergoes when traveling through a medium. This procedure is tested for a neodymium-doped yttrium aluminum garnet (Nd:YAG) crystal of 2.5 mm thickness. First the transmission spectrum of the sample is measured between 780 and 840 nm. This spectral region is large enough compared to the spectrum of the Ti:Sapphire laser, which has a center wavelength of 809 nm and a FWHM of 13.1 nm. The transmission spectrum as shown in Figure 6.3 is measured with a Shimadzu UV-1800 spectrometer.

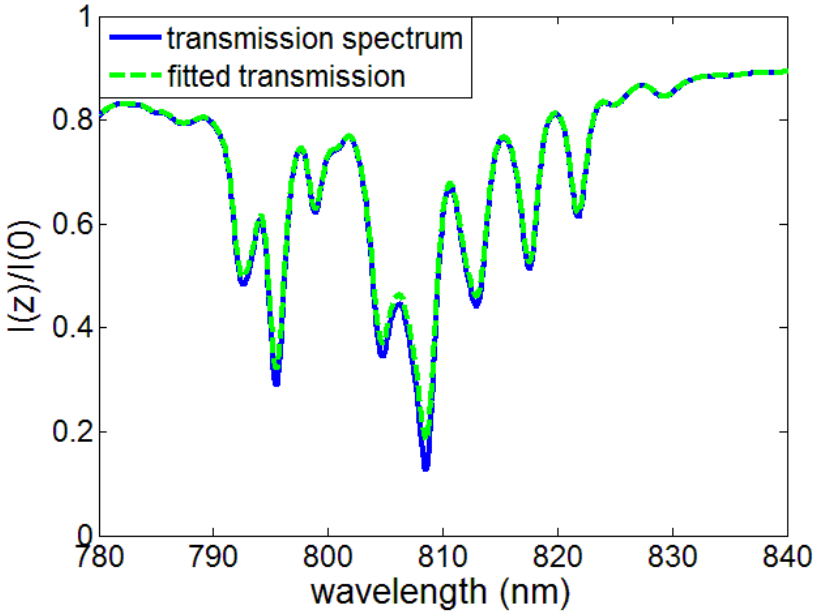

Figure 6.3: *measured (blue) and fitted (green) transmission spectrum.*

From the transmission spectrum the wavelength dependent absorption coefficient is calculated. The absorption coefficient, divided by the wavenumber $k = 2\pi/\lambda$, gives the complex part of the susceptibility. This obtained complex susceptibility is fitted with a sum of 60 damped harmonic oscillators as described by formula (6.21). The fitting is done using CMA-ES. The mean squared error between the fitted and measured complex value of the susceptibility is used as feedback parameter. The program uses the amplitude, center wavelength, and width of each oscillator as fitting parameters.

The fitted transmission spectrum I(z)/I(0) is show in Figure 6.3. By taking the real part of the fitted complex susceptibility we obtain the phase change caused by the narrow molecular resonances. This phase profile is shown in Figure 6.4. This phase profile is not complete as it describes only the phase change induced by resonances between 780 and 840 nm. There is also influence from broad electronic resonances with a center wavelength outside the range of 780 to 840 nm. The dispersion induced by these resonances is described by the Sellmeier equations[35] and can be added to the previously calculated phase profile. The Sellmeier equation for YAG is[36]:

$$n^2 - 1 = \frac{2.28200 \cdot \lambda^2}{\lambda^2 - 0.01185} + \frac{3.27644 \cdot \lambda^2}{\lambda^2 - 282.734} \qquad (6.26)$$

The phase change calculated from the Sellmeier equation is added to the phase delay induced by the sharp resonances to obtain the total phase delay.

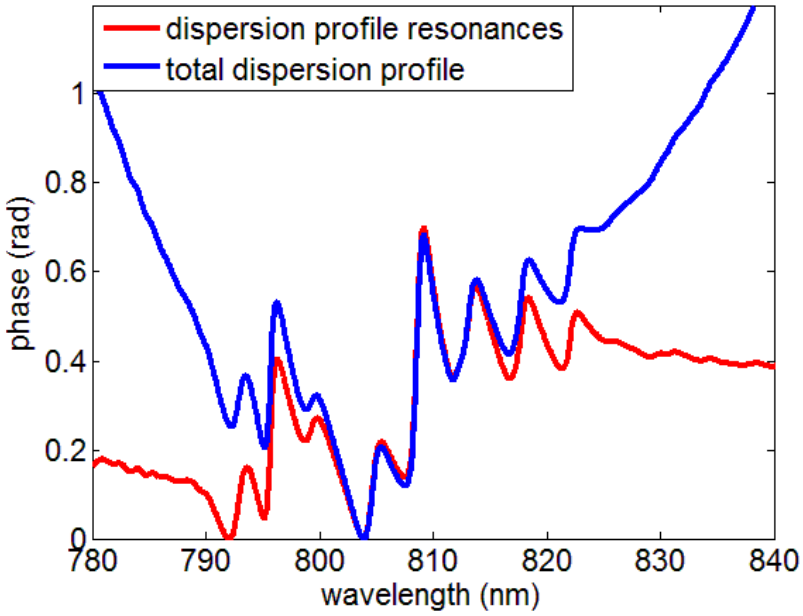

Figure 6.4: *phase delay resulting from the fitted resonances (red) and the total phase delay (blue).*

6.4 Chemical specificity through dispersion compensation

By compensating the phase delay induced by a compound of interest, chemical information from a sample can be obtained. First the phase profile that compensates dispersion in a compound of interest is calculated. In the setup the phase of the incoming light is shaped to compensate for this dispersion, after which the phase shaped light is sent through the sample. Behind the sample the two photon signal is measured by detection of SHG light generated in a nonlinear crystal. If the sample is of the same compound as the compound for which dispersion compensation shaping is done, a transform-limited pulse is obtained after the sample, which will result in a higher two photon signal. If the sample does not match the optimized compound, residual dispersion will lower the SHG intensity. This method can be applied to differentiate between compounds that have a distinctive phase delay profile.

6.5 Setup

In the setup the same Ti:Sapphire oscillator and shaper are used as in the CARS experiments, these are explained in chapter 3. A flip mirror is placed in the beam path after the shaper to redirect the beam from the CARS system to the sample for dispersion compensation measurements. A schematic overview of the setup is shown in Figure 6.5.

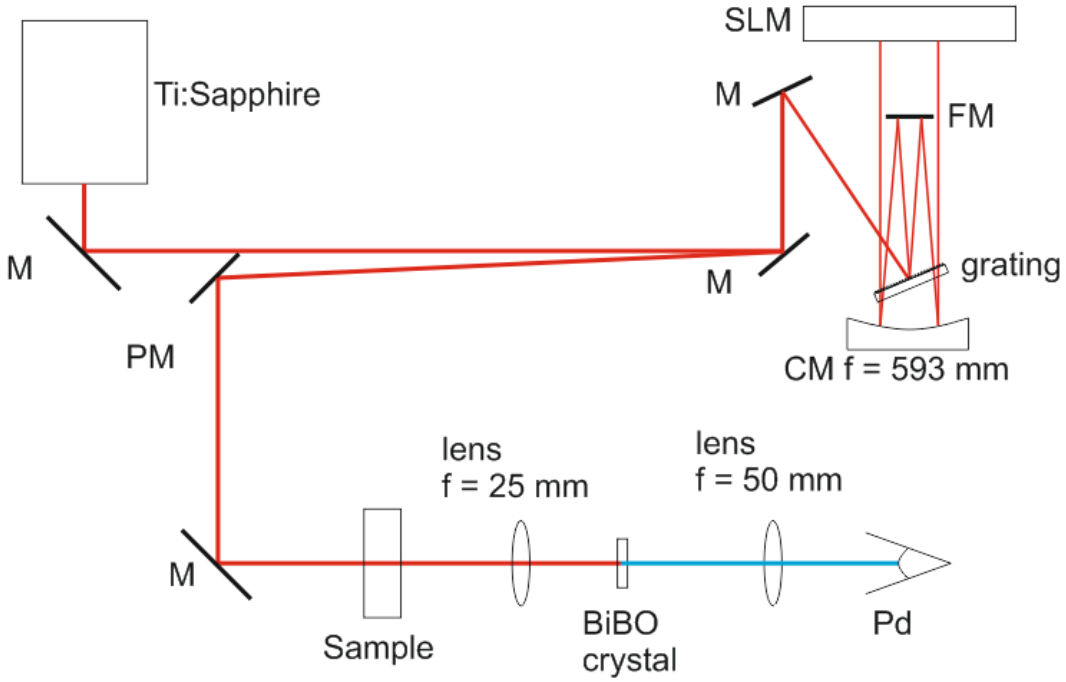

Figure 6.5: *Schematic representation of the setup. M = Mirror, PM = Pickoff Mirror, CM = Cylindrical Mirror, SLM = Spatial Light Modulator, PD = Photodiode*

The broadband laser pulses are generated with a Ti:Sapphire oscillator (KM-Labs). The spectrum has a center wavelength at 809 nm and a FWHM of 13.1 nm. The pulses have a temporal FWHM of roughly 80 fs and are emitted at 80 MHz repetition rate. The laser spectrum is shown in Figure 6.6. The laser pulses are shaped in a 4-f zero dispersion phase shaping setup as is discussed in chapter 3.3.

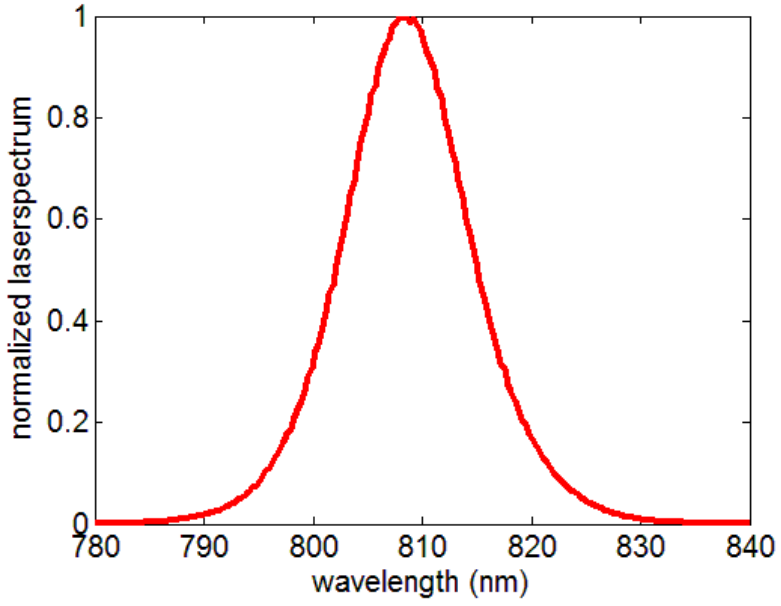

Figure 6.6: *measured normalized laser spectrum.*

With a pickoff mirror the shaped pulses are separated from the incoming laser beam and send to the sample. The sample on which the experiments are performed is a 2.5 mm thick Nd:YAG crystal. The light travels through the sample without focusing. Behind the sample is a 10 μm thick BiB_3O_6 crystal

placed in the focal distance between two lenses this is used for the excitation of SHG light. The excitation light is filtered from the SHG light with a filterset: (Thorlabs FB400-40, FGB37 and SP450). The transmitted SHG signal is detected with a silicon photodiode.

To compensate for any additional dispersion introduced by (transmissive) optics in the beampath, we perform an SHG optimization without the sample present. The resulting phase profile compensates any dispersion introduced by the optics in our setup and is added to any phase profiles that we apply.

7. Landscaping for chemical specificity

We have gathered both numerical and experimental data to investigate the obtainable specificity of our dispersion compensation method. In the first case the phase profile that compensates dispersion in a 2.5 mm thick Nd:YAG crystal is multiplied with a parameter c, this parameter is scanned from -3 to 3 $\varphi_{applied} = c \cdot \varphi_{opt}$. The obtained landscapes of the numerical simulation and the experiment can be seen in Figure 7.1 A and B respectively.

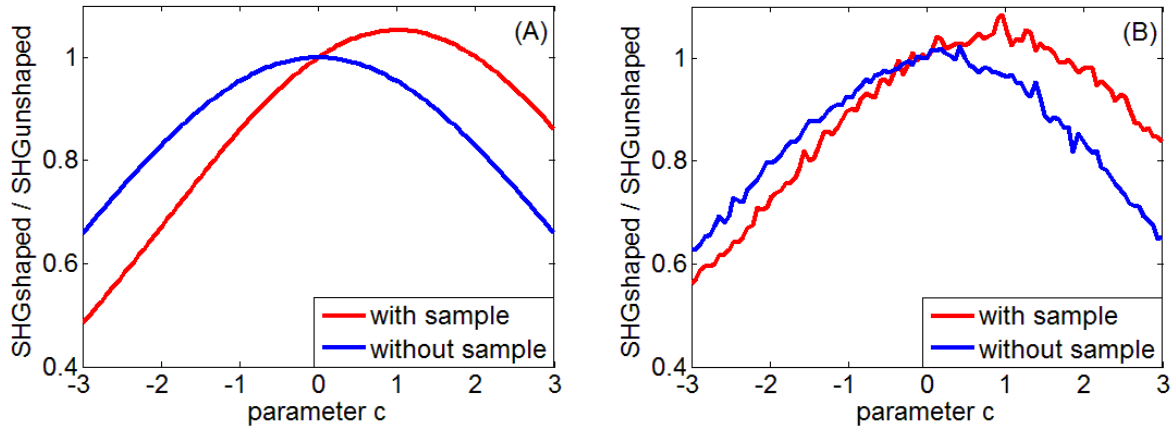

Figure 7.1: *(A) Numerical and (B) experimental 1D landscapes for a 2.5 mm Nd:YAG crystal.*

We can see from both figures that there is a clear shift in peak position from c = 0 to c = 1 with the sample present. This is the point where the phase change in the sample and the phase applied by the shaper compensate each other. The increase in signal between c = 0 and c = 1 is a factor of 1.05. When there is no sample present maximum intensity is obtained for c = 0. At c=0 the applied phase profile is zero, so the pulses remain transform limited. As the signals are normalized to the intensity obtained with an unshaped pulse, both graphs go through value 1 at point c = 0. As a result the graph for the experiment performed with a sample reaches a higher normalized value even though the absolute SHG signal is always higher when there is no sample present.

To further investigate the effect of phase shaping on the two photon signal we measured the 2D SHG landscape. In this measurement, the phase profiles that compensate dispersion resulting from the Sellmeier equations and dispersion due to sharp resonances are independently multiplied with parameters c and d. The total phase profile is described as:

$$\varphi_{applied} = c \cdot \varphi_{Sellmeier} + d \cdot \varphi_{absorption} \qquad (7.27)$$

The parameters c and d are both scanned from -3 to 3 while the SHG signal is recorded. This is used to create a 2-dimensional landscape where the intensity is recorded for each combination of parameters. The results of both the numerical simulations and the experiments both with and without a sample present can be seen in Figure 7.2. A star has been placed on the point where maximum signal is expected (c = 0, d = 0) without sample and (c = 1, d = 1) with sample.

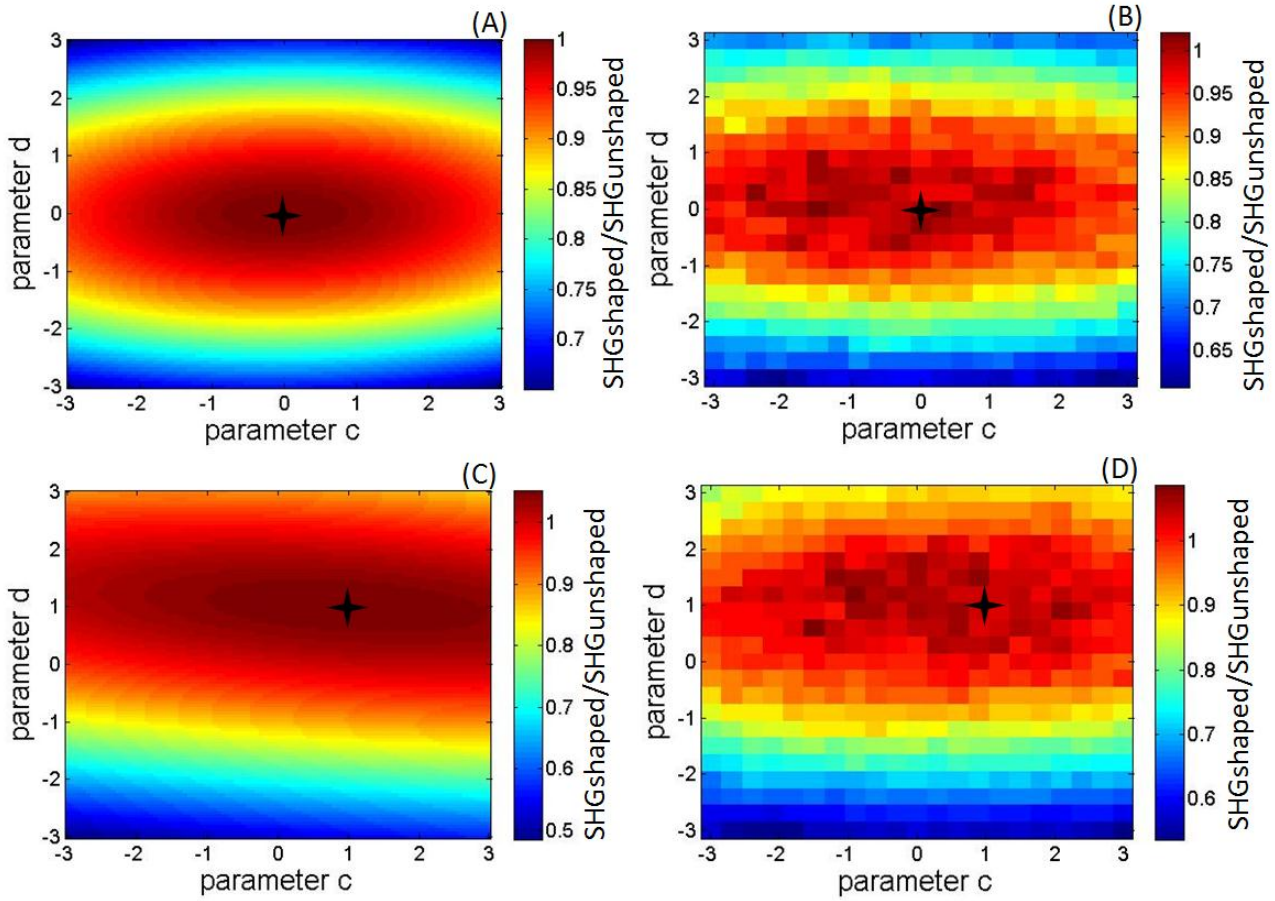

Figure 7.2: *(A) Numerical landscape without sample. (B) Experimental landscape without sample. (C) Numerical landscape with Nd:YAG. (D) Experimental landscape with Nd:YAG.*

We can see that when a sample is placed in the beam path, the shift in position is most pronounced along the vertical axis. This is the direction in which the amplitude of the phase profile for dispersion compensation for sharp resonances is scanned. The peak position clearly shifts from d = 0 to d = 1. The shift along the horizontal axis is less pronounced although we can see that there is a shift from c = 0 to c = 1. This shows that the chemical specificity is mainly obtained by compensating the phase changes due to the molecular resonances.

We can see that there are some deviations in the experimental landscapes compared to the numerical landscapes, mostly at the edges of the 2-dimensional landscapes. This is most likely caused by phase wrapping in the SLM. The SLM has a limited modulation depth, so 2π phase steps are used for larger applied phase delays. There is also some noise that is most obvious in the 1-dimensional landscape, which is a result of low frequency intensity fluctuations in the output of the excitation laser.

7.1 Discussion

We have presented a tool where spectral shaping is used in combination with a linear sample interaction to obtain chemical specificity. We exploit the fact that detection of the two photon signal behind the sample is influenced by a combination of the phase delay in the sample and the phase profile applied on the incoming pulses. This technique could be extended for use in an imaging technique where chemical selectivity is obtained based on a linear sample interaction. Advantages for such a technique are that detection can be performed on the integrated SHG signal without the use of a spectrometer or other imaging techniques. Furthermore with this technique there is no reason to focus the light in the sample which decreases the chance of damaging samples with high intensities.

There are several remaining challenges and possibilities for improvements. First it is possible to increase the sensitivity by using a broader spectrum. The broader spectrum will provide shorter light pulses that are stronger influenced by dispersion, further a broader spectrum can be influenced by a broader range of resonances and is thus selective for a broader spectral region. It is also possible to use a spectrum that is centered in the more selective NIR region where vibrational resonances are present. These vibrational resonances are more distinct and sharp and thus more selective for individual compounds.

The measurements providing 1D and 2D landscapes have shown that there is some noise on the obtained signal. This noise is mostly induced by fluctuations in the laser intensity as has been described in chapter 5.2. A more stable laser source will thus improve our obtained signal. Further it should be noted that it is crucial to have near transform limited excitation pulses. For this reason an optimization strategy is performed before the experiment is started to get a maximized SHG signal without the sample present. Even though this is done there will be some phase errors on the pulses which cause small differences between the simulated and experimental landscapes.

The fact that a linear sample interaction is used is interesting but it also provides a disadvantage. That is the signal's dependency on the sample's thickness and concentration. This limits this techniques possibilities for applications as it becomes difficult to image compounds with a varying thickness or concentration. It is possible to use multiple phase shapes that are calculated for different thicknesses of the same compound and to make separate images for these different thicknesses, which could be used to partially overcome this challenge.

Appendix

A. Spatial Light Modulator operation

The SLM that is used is a liquid crystal based SLM with a 1D array of 640 pixels. This SLM is used to control the phase profile of the light spectrum. The frequencies of the incoming light are spatially separated by a grating and focused on the SLM with a cylindrical mirror. The different frequencies are subsequently reflected from the backside of the SLM recombined by the cylindrical mirror and grating. The phase of the light is controlled by changing the refractive index in the individual pixels in the SLM. Operating the SLM is performed by applying a voltage over the birefringent liquid crystal pixel. This voltage causes a reorientation of the liquid crystal, which in turn causes change in the effective refractive index. The applied voltage ranges from 0 to 10 Volt and is discretized over 4096 drive levels. To obtain accurate phase modulation, it is important to calibrate the phase change as a result of the applied voltage. Furthermore, a calibration that relates each pixelnumber with the incident wavelength is required.

A.1. SLM alignment

This chapter covers the basic procedures for alignment of our pulse shaper setup[30]. For a schematic picture of the pulse shaping setup see Figure 3.2. First, a collimated beam (running parallel to the optical table) is sent into the shaper setup. The beam is reflected from a grating, where it is important to note that the diffraction plane of the grating is aligned parallel to the table. To achieve parallel alignment of the grating, the zero and first order diffraction are monitored and the grating is rotated until the diffraction orders are aligned in plane. As a result, the diffraction of the different frequency components in the laser pulse will also be in plane. The diffracted light is reflected via a folding mirror to a cylindrical mirror. The optical path distance between the grating and the cylindrical mirror is set to be equal to the focal length of the cylindrical mirror. This distance is adjusted by moving the folding mirror, which is placed on a translation stage. The light that is reflected from the cylindrical mirror propagates parallel to the table and is sent into the SLM. The SLM is placed at the focal distance of the cylindrical mirror, although it should be noted that this distance is less critical, as the dispersion is only affected by the distance between the cylindrical mirror and the grating.

A mirror is mounted on the backside of the SLM, and the light is reflected back at an angle slightly downward from the incoming light. The reflected light passes the cylindrical mirror, folding mirror and grating and is recombined in a collimated beam. The light exiting the shaper is sent to the other side of the optical table where the spatial separation between the incoming and exiting beams is large enough that they can be separated with a mirror. To ensure that there is no chirp in the shaper setup we measure the intensity of the SHG light generated in a BiB_3O_6 crystal. Corrections in the alignment of the shaper setup are made by optimizing the SHG signal. The most critical parameter is the position of the folding mirror, which determines the separation between the grating and cylindrical mirror.

Furthermore, the rotation angle of the cylindrical mirror needs to be parallel with the grating. Changing the rotation of the cylindrical mirror also changes the path of the reflected light. Therefore we monitor the light's back reflection from the SHG crystal with a camera and during rotation of the mirror we realign the mirror to keep the excitation light spot at the same place on the SHG crystal.

A.2. Wavelength calibration

The following procedure is used to calibrate the corresponding wavelength for each pixel of the SLM. A π phase step is applied on the SLM. The position of the phase step is scanned from pixel 1 to 640 and during this process the spectrum of the fundamental light is recorded in a spectrometer. Because of the sharp phase modulation at the position of the π step a part of the light at the position of the π step will be scattered out of the shaper. This results in a sharp dip in the recorded spectrum at the wavelength on which the step is applied. By recording the pixel number at which the step is applied and the wavelength at which the intensity dip occurs, we can make a wavelength-pixel calibration for

the SLM. Figure A.1 shows a typical measurement for a calibration. It can be seen that the pulse is centered between pixel number 150 and 300.

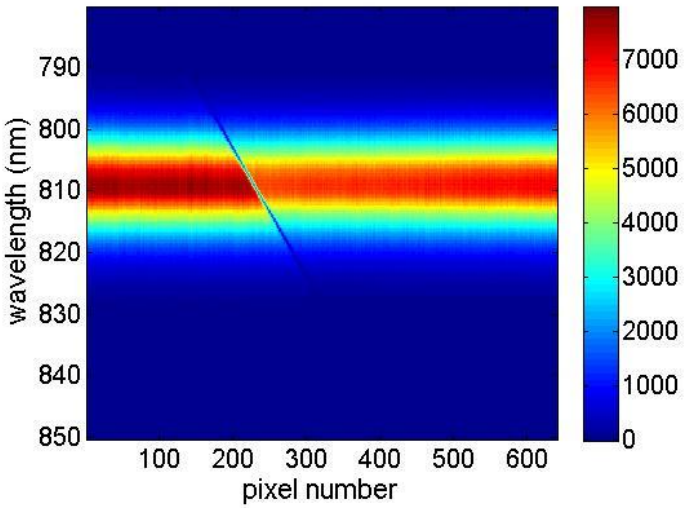

Figure A.1: *Intensity plot when applying a π phase step over the shaper, the step is centered at the pixel number shown on the horizontal axis.*

A.3. Drive level calibration

When considering the equations for amplitude and phase modulation and their dependence on the induced polarization change, it is possible to obtain a calibration that relates the masks drive levels to the applied phase and amplitude change. These equations are shown in chapter 3 formula (3.15) and (3.16).

Since the phase and amplitude modulation both depend on the polarization change in the SLM, the phase modulation and amplitude modulation are related to each other. This allows us to make a calibration for the applied phase change based on a measurement of amplitude shaping. Calibrating based on amplitude modulation is more straightforward, since it is much harder to accurately detect phase modulation compared to amplitude modulation. Each SLM mask is calibrated by scanning the drive levels from 0 to 4095 while keeping the other mask at zero modulation. During this process the fundamental spectrum of the shaped light is recorded and an intensity plot vs. drive level is made. From the measured normalized intensity the polarization change is retrieved, giving us a calibration for each mask. This procedure needs to be done for both masks individually, since there is a significant difference in the response of the individual masks to the applied drive level. Figure A.2 A and B show a typical measurement of intensity vs. drive level for both masks.

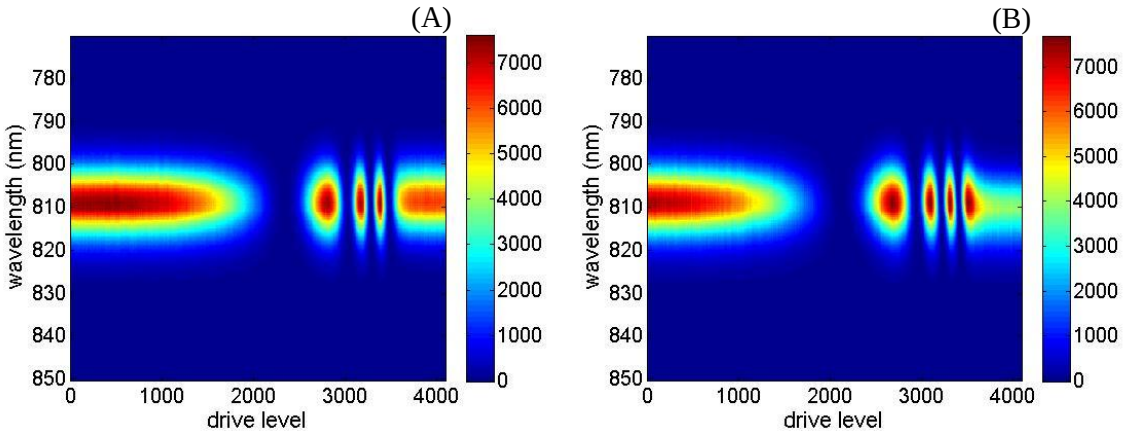

Figure A.2: *(A) Recorded intensity when scanning master mask drive levels. (B) Recorded intensity when scanning slave mask drive levels.*

A.4. Calibration verification

To verify the obtained calibration, several checks are performed. As a first check, the light is focused in a nonlinear crystal and the SHG signal is recorded in a spectrometer. A π phase step is applied on the shaper, and the step position is scanned over the shaper pixels corresponding to the laser spectrum. Two of these measurements are done, one with a positive π step and one with a negative π step. In the case of a correct alignment and calibration of the SLM the recorded 2-D spectrum for both measurements should be equal. If there are large intensity differences in the recorded spectra, the calibration or alignment is off. An example of this calibration verification experiment is shown in Figure A.3 (A, B and C).

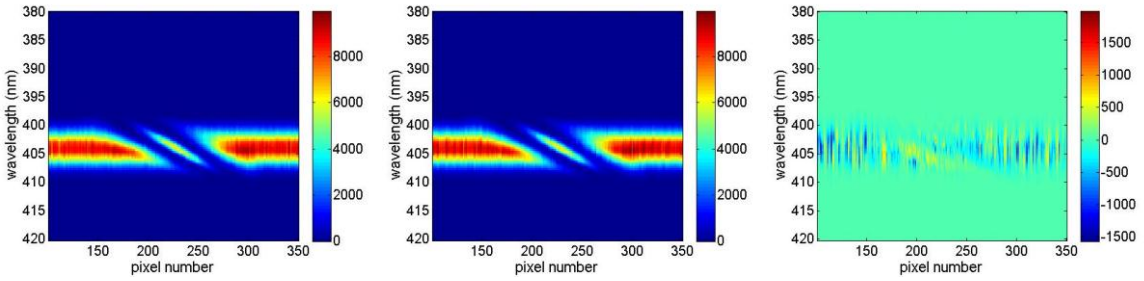

Figure A.3: *(A) SHG spectrum on scanning a positive π step. (B) SHG spectrum on scanning a negative π step. (C) Difference intensity from figure A and B.*

B. Frequency resolved optical gating

Frequency resolved optical gating (FROG) is a widely used method for measuring the spectrum, temporal behavior and spectral phase of ultrashort optical pulses[37]. We use SHG-FROG, which is one of many different FROG implementations[38]. In our system, FROG traces are mainly used to verify proper alignment of the shaping setup and laser cavity. A schematic of the setup that is used to obtain the FROG traces is shown in Figure B.4. The laser beam is divided into two different beampaths with a beamsplitter. Both optical paths combine with a lens in a nonlinear crystal. One of the paths has a length that is adjustable with a motorized translation stage, which allows us to tune the temporal overlap of the pulses in the crystal. Changing the temporal overlap influences the amount of excited second harmonic signal that is generated from the combination of the two beam paths. By recording the spectrum of the SHG signal for all these path length differences we obtain our FROG trace. From this FROG trace the original pulse's phase profile and spectrum can be retrieved. The only information that cannot be obtained is the direction of the phase profile (positive or negative), this is a result of the correlation experiment where the direction of time information is lost. This problem can be solved by placing a material with a known dispersion in the beam path and performing a second FROG trace.

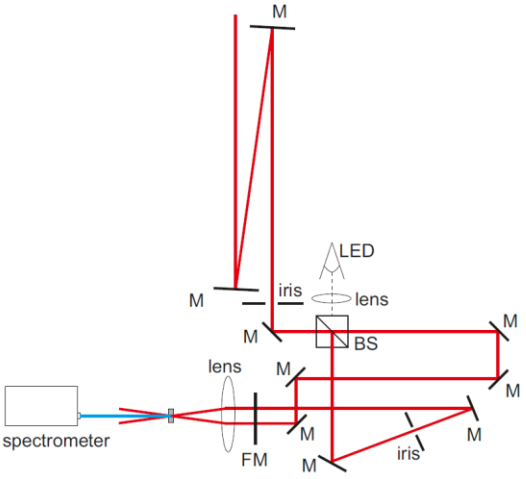

Figure B.4: *Schematic FROG setup.*

Some features have been implemented to help with alignment of the FROG setup. An iris is placed at the entrance of the FROG before the beamsplitter, and a second iris has been placed in one of the arms behind the beamsplitter. These irises can be used to align the beam with the two mirrors in front of the first iris. The laser beam generally loses a lot of intensity in the shaper setup which complicates a FROG measurement. Therefore it is generally easier to use the laser fundamental beam for alignment of the FROG and mark the appropriate positions for the irises, after which the beam from the shaper can be easily realigned.

Furthermore, a flip mirror has been place in the setup in front of the lens where both optical arms are combined. This mirror will reflect both beams back along the same path into the beamsplitter where on the other output port of the beamsplitter, a LED has been placed. This LED functions as a two photon detector. Raising the flip mirror allows us to use the setup as a fringe resolved autocorrelator, which is useful to find spatio-temporal overlap of beampaths[39]. We align the beams into the LED until we see an increase of two-photon signal, as a result of the small active area we know that there is some spatial overlap, now the translation stage can be adjusted until the signal rises and a fringe pattern can be observed at this point we have temporal and spatial overlap.

B.1. FROG traces

Here, several FROG traces of pulses that have different dominating orders of chirp are shown. FROG traces of near transform limited pulses, pulses with mostly 2nd order chirp and pulses with mostly 3th order chirp are presented. Identifying the highest remaining order of phase distortion can help in obtaining a correct alignment of the shaper setup.

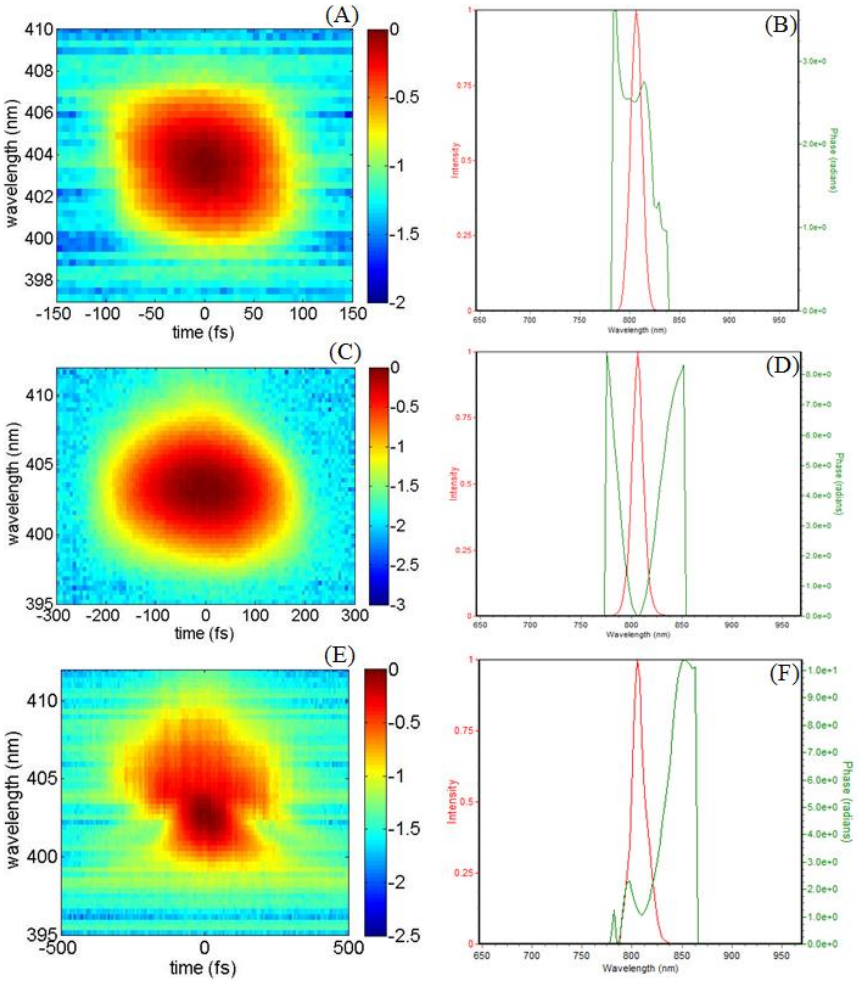

Figure A.5: *Measured FROG traces with different orders of chirp. Left: logarithmic intensity profile, right: retrieved phase and amplitude spectrum. (A and B) near transform limited pulse. (C and D) mainly 2nd order chirped pulse. (E and F) mainly 3th order chirped pulse.*

C. Overview of the setup

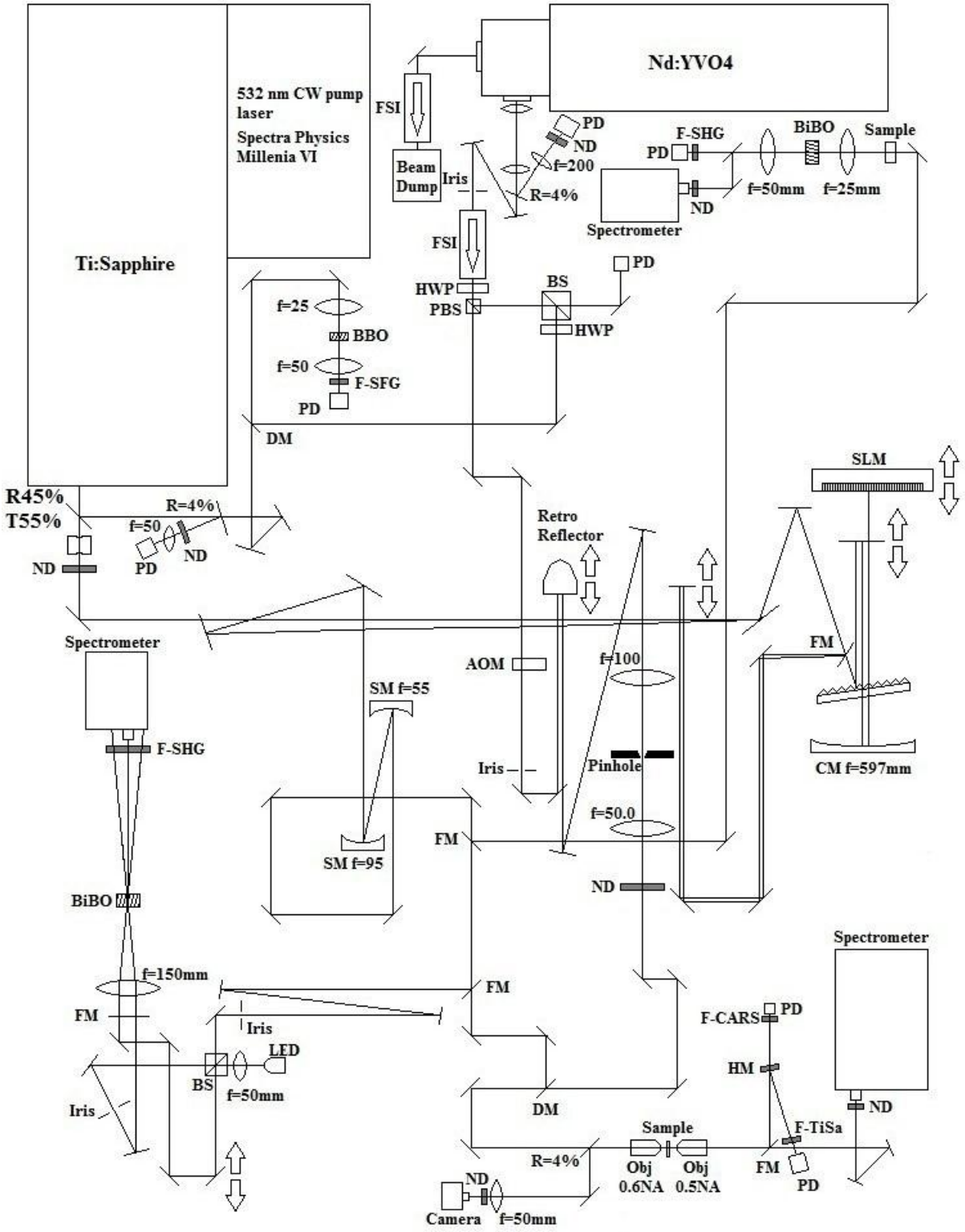

Figure A.6: *Schematic overview of the setup*

FM = flip mirror, DM = dichroic mirror, SM = spherical mirror, CM = spherical mirror, f = focal length (mm), cm = cylindrical mirror, BS = beam splitter, PBS = polarizing beam splitter, F-SHG/SFG/CARS = filter for SHG/SFG/CARS, PD = photodiode, ND = neutral density filter, AOM = acousto-optic modulator, SLM = spatial light modulator, HWP = half wave plate, FSI = free space isolator, BBO = barium borate crystal, BiBO = BiB_3O_6 bismuth borate crystal.

Acknowledgements

In the last ten months I enjoyed the opportunity to work within the Optical Sciences research group. I enjoyed the open character of the group, the scientific discussions and pleasant working environment. As a result of my work on a very interesting project I have learned a lot about scientific research. I want to thank Alexander for introducing me with the broadband CARS setup and his help in the lab. The daily supervision of this project was handled by Alexander and Herman. For this my thanks to you both as you always had time to answer any questions. Furthermore I want to thank Jeroen for his help with and knowledge of the electronics and laser synchronisation in the lab. Jennifer thank you for the opportunity to do my work within the Optical Sciences group. I have enjoyed the time spend within the group and would therefore like to thank all group members. Several people have helped me by reading and giving feedback on drafts of this thesis, for this I would like to thank Alexander, Herman, Gerwin and André. Of course thanks go to my family and friends for supporting me.

Bibliography

[1] A.C.W. van Rhijn, "Tailoring Pulses For coherent Raman Microscopy", PhD. thesis University of Twente, (2012).

[2] B.R. Masters, "The Development of Fluorescence Microscopy", Encyclopedia Of Life Sciences, 1-9 (2010).

[3] F. Zernike, "How I discovered phase contrast", Science **121**, 345-349 (1955).

[4] C V Raman, F.R.S. Indian, "A new radiation", J. Phys. **2** 387-398 (1928).

[5] N. Bloembergen, "The Stimulated Raman Effect", American Journal of Physics **35,** 989 1023 (1967).

[6] P. D. Maker, R. W. Terhune, "Study of Optical Effects Due to an Induced Polarization Third Order in the Electric Field Strength", Physical Review **137,** 801-818 (1964).

[7] R. F. Begley, A. B. Harvey, R. L. Byer, "Coherent anti-Stokes Raman spectroscopy", Appl. Phys. Lett. **25**, 387-390 (1974).

[8] M. D. Duncan, J. Reintjes, T. J. Manuccia, "Scanning coherent anti-Stokes Raman microscope", Optics letters **7**, 350-352 (1982).

[9] H.A. Haus, "Mode-Locking of Lasers", IEEE **6**, 1173-1185. (2000).

[10] D. Meshulach, Y. Silberberg, "Coherent quantum control of multiphoton transitions by shaped ultrashort optical pulses", The American Physical Society **60**, 1287-1292 (1999).

[11] J, Savolainen, "Coherent Control of Biomolecules", PhD. thesis University of Twente, (2008).

[12] J.R. Ferraro, K. Nakamoto, C.W. Brown, "Introductory Raman Spectroscopy", 2nd ed, pag 19-25 (2003).

[13] J.R. Ferraro, K. Nakamoto, C.W. Brown, "Introductory Raman Spectroscopy", 2nd ed, pag 7-9, (2003)

[14] D. Graf, F. Molitor, K. Ensslin, C. Stampfer, A. Jungen, C. Hierold, L. Wirtz, "Spatially Resolved Raman Spectroscopy of Single- and Few-Layer Graphene", Nano Letters **7**, 238-242 (2007).

[15] D.S. Knight, W.B. White, "Characterization of diamond films by Raman spectroscopy", Materials Research Society **4,** 385-393 (1989).

[16] C.W. Freudiger, W. Min, B. G. Saar, S. Lu, G.R. Holtom, C. He, J.C. Tsai, J.X. Kang, X.S. Xie, "Label-Free Biomedical Imaging with High Sensitivity by Stimulated Raman Scattering Microscopy", Science **322,** 1857-1861 (2008).

[17] A. Zumbusch, G.R. Holtom, X.S. Xie, "Three-Dimensional Vibrational Imaging by Coherent Anti-Stokes Raman Scattering", The American Physical Society **82**, 4142-4145 (1999).

[18] J. Cheng, A. Volkmer, L.D. Book, X.S. Xie, **"**Multiplex Coherent Anti-Stokes Raman Scattering Microspectroscopy and Study of Lipid Vesicles", Journal Physical Chemistry **106**, 8493-8498 (2002).

[19] N. Dudovich, D. Oron, Y. Silberberg, "Single-pulse coherently controlled nonlinear Raman spectroscopy and microscopy", Nature **418**, 512-514 (2002).

[20] A.C.W. van Rhijn, A. Jafarpour, J.L. Herek, H.L. Offerhaus, "Computational optimization of phase shaped CARS", Proceedings of SPIE **8226**, 2B 1-8 (2012).

[21] A. Volkmer, L.D. Book, X. Xie, "Time-resolved coherent anti-Stokes Raman scattering microscopy: Imaging based on Raman free induction decay", Applied Phyics letters **80**, 1505-1507 (2002).

[22] J.X. Cheng, L.D. Book, X.S. Xie, "Polarization coherent anti-Stokes Raman scattering microscopy", Optics Letters **26**, 1341-1343 (2001).

[23] A.Y. Chikishev, G.W. Lucassen, N.I. Koroteev, C. Otto, J. Grevet, "Polarization sensitive coherent anti-Stokes Raman scattering spectroscopy of the amide I band of proteins in solutions", Biophysics Journal **63,** 976-985 (1992).

[24] M. Jurna, J. P. Korterik, C. Otto, J. L. Herek, H. L. Offerhaus, "Vibrational Phase Contrast Microscopy by Use of Coherent Anti-Stokes Raman Scattering", The American Physical Society PRL **103**, 043905 1-4 (2009).

[25] D. A. Kleinman, "Nonlinear Dielectric Polarization in Optical Media", Physical Review **126**, 1977- 1979 (1962).

[26] D. Sprunken, “A 2D Spatial Light Modulator for spatio-temporal shaping”, Msc. Thesis University of Twente, (2008).
[27] Cambridge Recearch & Instumentation, Inc, “SLM Spatial Light Modulator User’s Manual Rev. 1.5”, (2010)
[28] A. C. W. van Rhijn, M. Jurna, A. Jafarpour, J. L. Herek and H. L. Offerhaus, “Phase-shaping strategies for coherent anti-Stokes Raman scattering”, Journal of Raman Spectroscopy, **42**, 1859-1863 (2011).
[29] F. Salin, A. Brun, “Dispersion compensation for femtosecond pulses using high-index prisms”, Journal Applied Physics **61**, 4736-4739 (1987).
[30] A. M. Weiner, “Femtosecond pulse shaping using spatial light modulators”, Review Of Scientific Instruments **71**, 1929-1960 (2000).
[31] J. D. McMullen, “Analysis of compression of frequency chirped optical pulses by a strongly dispersive grating pair”, Applied Optics **18**, 737-741 (1979).
[32] R. L. Fork, O. E. Martinez, J. P. Gordon, “Negative dispersion using pairs of prisms”, Optics Letters **9**, 150-152 (1984).
[33] T. Baumert, T. Brixner, V. Seyfried, M. Strehle, G. Gerber, “Femtosecond pulse shaping by an evolutionary algorithm with feedback”, Applied Physics B **65**, 779-782 (1997).
[34] R. W. Boyd, “Nonlinear Optics”, 2nd ed, pag 158-161, (2003)
[35] W. Sellmeier, “Zur erklärung der abnormen farbenfolge im spectrum einiger substanze”, Annalen der Physik **219**, 272-282 (1871).
[36] D.E. Zelmon, D.L. Small, R. Page, “Refractive-index measurements of undoped yttrium aluminum garnet from 0.4 to 5.0 μm”, Applied Optics **37**, 4933-4935 (1998).
[37] D.J. Kane, R. Trebino, “Characterisation of Arbitrary Femtosecond Pulses Using Frequency-Resolved Optical Gating”, IEEE Journal of Quantum Electronics **29**, 571-579 (1993).
[38] R. Trebino, K.W. DeLong, D.N. Fittinghoff, J.N. Sweetser, M.A. Krumbügel, B.A. Richman, “Measuring ultrashort laser pulses in the time-frequency domain using frequency-resolved optical gating”, Review Of Scientific Instruments **68**, 3277-3295 (1997).
[39] T. Mindl, P. Hefferle, S. Schneider, F. Dorr, “Characterisation of a Train of Subpicosecond Laser Pulses by Fringe Resolved Autocorrelation Measurements”, Applied Physics B **31**, 201-207 (1983).